

JAX-Fluids 2.0: Towards HPC for Differentiable CFD of Compressible Two-phase Flows

Deniz A. Bezgin^{a,1,*}, Aaron B. Buhendwa^{a,1,*}, Nikolaus A. Adams^{a,b},

^a*Technical University of Munich, School of Engineering and Design, Chair of Aerodynamics and Fluid Mechanics, Boltzmannstraße 15, 85748 Garching bei München, Germany*

^b*Technical University of Munich, Munich Institute of Integrated Materials, Energy and Process Engineering, Lichtenbergstraße 4a, 85748 Garching bei München, Germany*

Abstract

In our effort to facilitate machine learning-assisted computational fluid dynamics (CFD), we introduce the second iteration of JAX-Fluids. JAX-Fluids is a Python-based fully-differentiable CFD solver designed for compressible single- and two-phase flows. In this work, the first version is extended to incorporate high-performance computing (HPC) capabilities. We introduce a parallelization strategy utilizing JAX primitive operations that scales efficiently on GPU (up to 512 NVIDIA A100 graphics cards) and TPU (up to 1024 TPU v3 cores) HPC systems. We further demonstrate the stable parallel computation of automatic differentiation gradients across extended integration trajectories. The new code version offers enhanced two-phase flow modeling capabilities. In particular, a five-equation diffuse-interface model is incorporated which complements the level-set sharp-interface model. Additional algorithmic improvements include positivity-preserving limiters for increased robustness, support for stretched Cartesian meshes, refactored I/O handling, comprehensive post-processing routines, and an updated list of state-of-the-art high-order numerical discretization schemes. We verify newly added numerical models by showcasing simulation results for single- and two-phase flows, including turbulent boundary layer and channel flows, air-helium shock bubble interactions, and air-water shock drop interactions. JAX-Fluids 2.0 is released under the GNU GPLv3 license and made available on GitHub at <https://github.com/tumaer/JAXFLUIDS>.

Keywords: Computational fluid dynamics, Machine learning, Differential programming, High performance computing, JAX, Navier-Stokes equations, Turbulence, Level-set, Diffuse-interface, Two-phase flows

PROGRAM SUMMARY

Program Title: JAX-Fluids

Developer's repository link: (<https://github.com/tumaer/JAXFLUIDS>)

*Corresponding author

Email addresses: deniz.bezgin@tum.de (Deniz A. Bezgin), aaron.buhendwa@tum.de (Aaron B. Buhendwa), nikolaus.adams@tum.de (Nikolaus A. Adams)

¹Both authors contributed equally.

Licensing provisions: GPLv3

Programming language: Python, JAX

Supplementary material: Source code; Example scripts; Videos.

Journal reference of previous version:

- D. A. Bezgin, A. B. Buhendwa, N. A. Adams, JAX-Fluids: A fully-differentiable high-order computational fluid dynamics solver for compressible two-phase flows, *Computer Physics Communications* 282 (2022) 108527.

Does the new version supersede the previous version?: Yes

Reasons for the new version: New features and updates of the CFD solver

Summary of revisions:

- JAX primitives-based parallelization for GPU and TPU clusters
- Automatic differentiation through distributed simulations
- Diffuse-interface model for two-phase flows
- Positivity-preserving interpolation and flux limiters
- Support for stretched Cartesian meshes
- Extended list of numerical discretization schemes
- Performance improvements
- Revised I/O handling

Nature of problem: The compressible Navier-Stokes equations describe continuum-scale fluid flows which may exhibit complex phenomena such as shock waves, material interfaces, and turbulence. The accurate numerical solution of fluid flows is computationally expensive and, therefore, requires high performance computing (HPC) architectures. To this end, machine learning (ML), in particular differentiable programming, is continuously being explored as a tool to accelerate conventional computational fluid dynamics (CFD). With the second iteration of JAX-Fluids, we provide a comprehensive differentiable CFD code that scales efficiently on HPC systems and seamlessly integrates ML models. Furthermore, JAX-Fluids is capable of simulating highly complex flow physics such as supersonic boundary layer flow or interactions of shock waves with material interfaces.

Solution method: JAX-Fluids is a finite-volume solver which uses low-dissipative high-order shock capturing schemes in combination with approximate Riemann solvers. Two-phase flows can be simulated using the sharp-interface level-set method or the diffuse-interface five-equation model. The code is written in Python and builds on the JAX library. The JAX backend allows the computation of automatic differentiation gradients. We use a homogenous domain decomposition ansatz to implement the parallelization. An object-oriented programming style and a modular design philosophy allow exchanging numerical schemes and integrating custom subroutines.

Additional comments including Restrictions and Unusual features: JAX-Fluids runs on CPUs, GPUs, and TPUs in single- and multi-device settings. JAX-Fluids requires open-source third-party Python libraries which are automatically installed. The solver has been tested on Linux and macOS operating systems.

1. Introduction

The numerical solution of partial differential equations (PDEs) is key to simulating and understanding physical systems. The solution of high-dimensional complex PDEs requires vast computational resources provided by high-performance computing (HPC). Algorithms aimed at solving PDEs on HPC systems have traditionally been written in low-level programming languages like Fortran or C/C++. In recent years, machine learning (ML)-assisted numerical schemes have been developed for the solution of PDEs. The field of fluid mechanics in particular benefits from ML-assisted modeling due to the nonlinearity and multiscale nature of the underlying physics as well as its data-rich character [1, 2]. As ML libraries are predominantly used in Python, however, the integration of ML into conventional PDE solvers and the joint application on HPC systems requires novel simulation frameworks.

Differentiable solvers have gained increased attention in engineering and in the physical sciences due to their promise of bridging the aforementioned gap between computational physics and machine learning. In particular, differentiable solvers ensure automatic differentiation (AD) [3] of the entire algorithmic representation of the chosen numerical approximation of the PDE evolution law. The training of data-driven models with such gradients is referred to as *end-to-end optimization*. End-to-end optimized models generally allow stable inference over long prediction horizons. The interest in differentiable simulators has also been fueled by the development of powerful general purpose AD libraries, such as TensorFlow [4], PyTorch [5], and JAX [6]. Recent applications of differentiable solvers include computational fluid dynamics (e.g., for molecular dynamics simulations [7], incompressible single-phase flows [8, 9], and Lattice Boltzmann methods [10]), structural mechanics (e.g., [11]), etc.

We reiterate some of the requirements we deem essential for next-generation physics solvers:

1. Rapid prototyping capability in high-level programming languages like Python,
2. algorithms which scale efficiently on modern HPC architectures (e.g., CPU, GPU, and TPU clusters),
3. seamless integration of machine learning models into physics solver frameworks,
4. differentiable algorithms which allow end-to-end optimization of data-driven models.

In light of the aforementioned points, we have proposed JAX-Fluids [12] as a fully-differentiable computational fluid dynamics (CFD) solver for compressible two-phase flows. JAX-Fluids is build upon the JAX-based [6, 13] implementation of the popular NumPy package [14], making it easy and intuitive to use. The JAX backend [6, 13] allows automatic differentiation through every subroutine of our solver, and it provides capabilities to run on CPU, GPU, and TPU accelerators.

In this work, we introduce the second iteration of the JAX-Fluids CFD framework. While the first release of JAX-Fluids was restricted to a single device, JAX-Fluids 2.0 has been developed for use on distributed HPC architectures. A parallelization strategy using only JAX primitives allows obtaining automatic differentiation gradients in distributed settings. In particular, JAX-Fluids 2.0

supports single-host and multi-host settings. Additionally, the two-phase modeling capabilities have been enhanced by a diffuse-interface module. For two-phase simulations, users can now choose between a level-set-based sharp-interface model [15, 16, 17] and a five-equation diffuse-interface model [18, 19, 20, 21]. Single- and two-phase modules are enhanced by positivity-preserving techniques for increased robustness. JAX-Fluids 2.0 is complemented by performance improvements throughout the entire source code, support for stretched Cartesian meshes, an updated list of discretization schemes, improved I/O-handling, and comprehensive post-processing routines. JAX-Fluids 2.0 is capable of performing direct numerical simulations of compressible, wall-bounded turbulence and highly resolved simulations of complex shock-interface interactions. The computation of gradients obtained by automatic differentiation shows stable behavior through extended integration trajectories across multiple devices.

Differentiable CFD solvers like JAX-Fluids may contribute to a plethora of data-driven applications in the context of fluid mechanics. We highlight three fields which we deem especially relevant.

1. **End-to-end Optimization of Surrogate Models:** Up to now, many machine learning models for CFD have been optimized *offline*, i.e., outside the CFD solver. Offline trained models may become unstable during long rollout trajectories due to error accumulation (e.g., [22]). Online training may alleviate this issue as models observe PDE dynamics during training and have to account for their own prediction errors [23, 8, 24].
2. **Inverse Problems:** An important inverse problem in fluid mechanics is flow reconstruction from incomplete information (e.g., sparse measurements). Physics-informed neural networks (PINNs) have been used extensively in this context [25, 26, 27]. However, recently the optimization of a discrete loss (ODIL) framework was introduced which utilizes differentiable solvers [28].
3. **Uncertainty Quantification:** Differentiable physics simulators can be used in probabilistic frameworks to model and quantify uncertainty.

The manuscript is structured as follows. In section 2, we introduce the single-phase Navier-Stokes equations, the level-set formalism, and the five-equation diffuse-interface model. Section 3 discusses the numerical discretization of the aforementioned equations. We introduce the JAX-based parallelization strategy of JAX-Fluids in Section 4. Verification of the numerical models and the automatic differentiation gradients is presented in Sections 5 and 6, respectively. In Section 7, we analyze the parallel performance of JAX-Fluids on GPU and TPU clusters. Section 8 provides a summary of the achievements and gives concluding remarks.

2. Physical model

JAX-Fluids solves compressible single-phase and two-phase flows. In this section, we introduce the underlying governing equations. Two-phase flows in JAX-Fluids can be solved by a level-set-based

sharp-interface model or the five-equation diffuse-interface model. We detail both two-phase modeling approaches.

The state of the fluid at any position $\mathbf{x} = [x, y, z]^T = [x_1, x_2, x_3]^T$ in the flow field at time t can be described either by the vector of primitive variables \mathbf{W} or by the vector of conservative variables \mathbf{U} . Both representations of the fluid state are equivalent, i.e., $\mathbf{W} = \mathcal{L}_{\mathbf{U} \rightarrow \mathbf{W}}(\mathbf{U})$, and $\mathbf{U} = \mathcal{L}_{\mathbf{W} \rightarrow \mathbf{U}}(\mathbf{W})$. The compressible Navier-Stokes equations in symbolic form for the vector of conservative variables are

$$\frac{\partial \mathbf{U}}{\partial t} + \frac{\partial \mathbf{F}^c(\mathbf{U})}{\partial x} + \frac{\partial \mathbf{G}^c(\mathbf{U})}{\partial y} + \frac{\partial \mathbf{H}^c(\mathbf{U})}{\partial z} = \frac{\partial \mathbf{F}^d(\mathbf{U})}{\partial x} + \frac{\partial \mathbf{G}^d(\mathbf{U})}{\partial y} + \frac{\partial \mathbf{H}^d(\mathbf{U})}{\partial z} + \sum_i \mathbf{S}_i(\mathbf{U}). \quad (1)$$

\mathbf{F}^c , \mathbf{G}^c , and \mathbf{H}^c denote the convective fluxes in x -, y - and z -direction. Analogously, \mathbf{F}^d , \mathbf{G}^d , and \mathbf{H}^d denote the dissipative fluxes in the three spatial dimensions. The right-hand side is complemented by the sum of all source terms $\sum_i \mathbf{S}_i(\mathbf{U})$.

2.1. Single-phase model

For single-phase flows, the primitive variables are the fluid density ρ , the velocity components u , v , and w (in x -, y -, and z -direction, respectively), and the pressure p . $\mathbf{u} = [u, v, w]^T = [u_1, u_2, u_3]^T$ is the velocity vector. $E = \rho e + \frac{1}{2} \rho \mathbf{u} \cdot \mathbf{u}$ denotes the total energy of the fluid. The vectors of primitive and conservative variables are given as

$$\mathbf{W} = \begin{bmatrix} \rho \\ u \\ v \\ w \\ p \end{bmatrix}, \quad \mathbf{U} = \begin{bmatrix} \rho \\ \rho u \\ \rho v \\ \rho w \\ E \end{bmatrix}, \quad (2)$$

and the convective fluxes are

$$\mathbf{F}^c(\mathbf{U}) = \begin{bmatrix} \rho u \\ \rho u^2 + p \\ \rho u v \\ \rho u w \\ u(E + p) \end{bmatrix}, \quad \mathbf{G}^c(\mathbf{U}) = \begin{bmatrix} \rho v \\ \rho v u \\ \rho v^2 + p \\ \rho v w \\ v(E + p) \end{bmatrix}, \quad \mathbf{H}^c(\mathbf{U}) = \begin{bmatrix} \rho w \\ \rho w u \\ \rho w v \\ \rho w^2 + p \\ w(E + p) \end{bmatrix}. \quad (3)$$

The dissipative fluxes describe viscous effects and heat conduction.

$$\mathbf{F}^d(\mathbf{U}) = \begin{bmatrix} 0 \\ \tau^{11} \\ \tau^{12} \\ \tau^{13} \\ \sum_i u_i \tau^{1i} - q_1 \end{bmatrix}, \quad \mathbf{G}^d(\mathbf{U}) = \begin{bmatrix} 0 \\ \tau^{21} \\ \tau^{22} \\ \tau^{23} \\ \sum_i u_i \tau^{2i} - q_2 \end{bmatrix}, \quad \mathbf{H}^d(\mathbf{U}) = \begin{bmatrix} 0 \\ \tau^{31} \\ \tau^{32} \\ \tau^{33} \\ \sum_i u_i \tau^{3i} - q_3 \end{bmatrix}. \quad (4)$$

The stresses τ^{ij} are given by

$$\tau^{ij} = \mu \left(\frac{\partial u_i}{\partial x_j} + \frac{\partial u_j}{\partial x_i} \right) - \frac{2}{3} \mu \delta_{ij} \frac{\partial u_k}{\partial x_k}, \quad (5)$$

where μ is the dynamic viscosity. The energy flux vector $\mathbf{q} = [q_1, q_2, q_3]^T$ is expressed via Fourier's heat conduction law, $\mathbf{q} = -\lambda \nabla T$, where λ is the heat conductivity.

2.2. Level-set model

The level-set model [15, 16] (LSM) is a sharp-interface method and uses a signed distance function ϕ to track the interface. The interface location is implicitly given by its zero level-set. The two phases are distinguished by its sign. The system of equations described in the previous subsection 3.5, i.e., Eqs. (2),(3), and (4) hold for both phases separately. In addition, the level-set function is evolved according to

$$\frac{\partial \phi}{\partial t} = -\mathbf{u}_\Gamma \cdot \nabla \phi = \mathcal{R}_{LSA}, \quad (6)$$

where \mathbf{u}_Γ is the interface velocity.

2.3. Diffuse-interface model

In the five-equation diffuse-interface model (DIM) [18, 19], the interface is artificially thickened over a finite region. We solve a separate continuity equation for each phase ($\alpha_1 \rho_1$ and $\alpha_2 \rho_2$ denote the phase masses for each fluid), a momentum equation, an energy equation, and a volume fraction

equation for either one of the two fluids. The primitive and conservative variables are

$$\mathbf{W} = \begin{bmatrix} \alpha_1 \rho_1 \\ \alpha_2 \rho_2 \\ u \\ v \\ w \\ p \\ \alpha_1 \end{bmatrix}, \quad \mathbf{U} = \begin{bmatrix} \alpha_1 \rho_1 \\ \alpha_2 \rho_2 \\ \rho u \\ \rho v \\ \rho w \\ E \\ \alpha_1 \end{bmatrix}. \quad (7)$$

The density of the mixture $\rho = \alpha_1 \rho_1 + \alpha_2 \rho_2$, and the volume fraction of the second fluid $\alpha_2 = 1 - \alpha_1$. The convective fluxes in the three spatial dimensions are given as

$$\mathbf{F}^c(\mathbf{U}) = \begin{bmatrix} \alpha_1 \rho_1 u \\ \alpha_2 \rho_2 u \\ \rho u^2 + p \\ \rho uv \\ \rho uw \\ u(E + p) \\ \alpha_1 u \end{bmatrix}, \quad \mathbf{G}^c(\mathbf{U}) = \begin{bmatrix} \alpha_1 \rho_1 v \\ \alpha_2 \rho_2 v \\ \rho v u \\ \rho v^2 + p \\ \rho vw \\ v(E + p) \\ \alpha_1 v \end{bmatrix}, \quad \mathbf{H}^c(\mathbf{U}) = \begin{bmatrix} \alpha_1 \rho_1 w \\ \alpha_2 \rho_2 w \\ \rho w u \\ \rho w v \\ \rho w^2 + p \\ w(E + p) \\ \alpha_1 w \end{bmatrix}. \quad (8)$$

Using the convective flux terms in Eq. (8), we recast the (non-conservative) volume fraction transport equation,

$$\frac{\partial \alpha_1}{\partial t} + \mathbf{u} \cdot \nabla \alpha_1 = 0,$$

into its equivalent conservative form,

$$\frac{\partial \alpha_1}{\partial t} + \nabla \cdot (\alpha_1 \mathbf{u}) = \alpha_1 \nabla \cdot \mathbf{u}, \quad (9)$$

see [29, 20]. The resulting source term is accounted for on the right-hand side,

$$\mathbf{S}_\alpha = \begin{bmatrix} 0 \\ 0 \\ 0 \\ 0 \\ 0 \\ 0 \\ \alpha_1 \nabla \cdot \mathbf{u} \end{bmatrix}. \quad (10)$$

2.4. Equation of state

The system of equations (1) is closed by an equation of state (EOS). Throughout this work we employ the stiffened gas equation of state [30].

$$p = (\gamma - 1) \rho e - \gamma p_\infty \quad (11)$$

$$c = \sqrt{\frac{\gamma (p + p_\infty)}{\rho}} \quad (12)$$

The stiffened gas equation has two parameters: γ is the ratio of specific heats, and p_∞ is the background pressure. For vanishing background pressures ($p_\infty = 0$) the stiffened gas EOS reduces to the ideal gas law.

For the five-equation model, we consider the mixture of two fluids. Each fluid is governed by its stiffened gas EOS, i.e., we have $(\gamma_1, p_{1,\infty})$ and $(\gamma_2, p_{2,\infty})$. The isobaric closure [18] gives an explicit analytic expression for the EOS parameters of the mixture (γ, p_∞) .

$$\frac{1}{\gamma - 1} = \frac{\alpha_1}{\gamma_1 - 1} + \frac{1 - \alpha_1}{\gamma_2 - 1} \quad (13)$$

$$\frac{\gamma p_\infty}{\gamma - 1} = \frac{\alpha_1 \gamma_1 p_{1,\infty}}{\gamma_1 - 1} + \frac{(1 - \alpha_1) \gamma_2 p_{2,\infty}}{\gamma_2 - 1} \quad (14)$$

2.5. Material properties

For viscous simulations, we require models for dynamic viscosity and thermal conductivity. In this work, we use two different models for the dynamic viscosity μ . The first is a simple power law,

$$\mu = \mu_{ref} \left(\frac{T}{T_{ref}} \right)^{0.7}, \quad (15)$$

where μ_{ref} is the dynamic viscosity at the reference temperature T_{ref} . The second is the well known Sutherland's law [31],

$$\mu = \mu_{ref} \left(\frac{T}{T_{ref}} \right)^{1.5} \frac{T_{ref} + C}{T + C}, \quad (16)$$

where C is Sutherland's constant. In both cases, the thermal conductivity λ can be determined using the assumption of a constant Prandtl number,

$$\lambda = \frac{Pr}{\mu c_p}. \quad (17)$$

Here, c_p denotes the specific heat capacity at constant pressure.

3. Numerical models

The aforementioned system of PDEs (1) is discretized on a Cartesian grid using the finite-volume formulation. Cell-averaged quantities (denoted by an overbar) are updated using cell face fluxes which are calculated from a high-order Godunov-type scheme [32].

3.1. Computational domain, grid, and boundary conditions

The computational domain is partitioned in $N_x \times N_y \times N_z$ cuboid finite volumes. Figure 1 depicts an exemplary computational domain including the nomenclature for the boundary locations at the corresponding axis directions. The finite-volume cell indexed by (i, j, k) is associated with the volume $x, y, z \in \left[x_{i-\frac{1}{2},j,k}, x_{i+\frac{1}{2},j,k} \right] \times \left[y_{i,j-\frac{1}{2},k}, y_{i,j+\frac{1}{2},k} \right] \times \left[z_{i,j,k-\frac{1}{2}}, z_{i,j,k+\frac{1}{2}} \right]$, where i, j , and k are the indices in x -, y -, and z -direction, respectively. The cell faces of cell (i, j, k) are located at $x_{i\pm\frac{1}{2},j,k}$, $y_{i,j\pm\frac{1}{2},k}$, and $z_{i,j,k\pm\frac{1}{2}}$, and the cell center position is given by $\left[\frac{x_{i-\frac{1}{2},j,k} + x_{i+\frac{1}{2},j,k}}{2}, \frac{y_{i,j-\frac{1}{2},k} + y_{i,j+\frac{1}{2},k}}{2}, \frac{z_{i,j,k-\frac{1}{2}} + z_{i,j,k+\frac{1}{2}}}{2} \right]$. The cell sizes in the three spatial dimensions are $\Delta x_{i,j,k} = x_{i+\frac{1}{2},j,k} - x_{i-\frac{1}{2},j,k}$, $\Delta y_{i,j,k} = y_{i,j+\frac{1}{2},k} - y_{i,j-\frac{1}{2},k}$, and $\Delta z_{i,j,k} = z_{i,j,k+\frac{1}{2}} - z_{i,j,k-\frac{1}{2}}$, and the cell volume is calculated as $\Delta V_{i,j,k} = \Delta x_{i,j,k} \Delta y_{i,j,k} \Delta z_{i,j,k}$. JAX-Fluids supports arbitrary one-dimensional mesh-stretching such that the cell face positions (and, therefore, the cell sizes) can be functions of the corresponding spatial index. Exemplary mesh stretchings are given in Appendix B. If a homogenous grid spacing is used, we indicate cell sizes simply by Δx , Δy , and Δz . For the isotropic case, we have $\Delta x = \Delta y = \Delta z$.

To evaluate spatial stencils close to and at the outer faces of the computational domain, we make use of halo cells. In practice, an arbitrary buffer therefore has the shape $[N_x + 2N_h, N_y + 2N_h, N_z + 2N_h]$. The number of halo cells N_h depend on the structure of the utilized spatial stencils, which we will detail in the following subsections. To enforce symmetry and periodicity at the boundaries, halo cells are inferred from the internal cells in a straight-forward fashion. To impose Dirichlet boundary conditions, we simply assign the cell center values of the halo cells to the desired values.

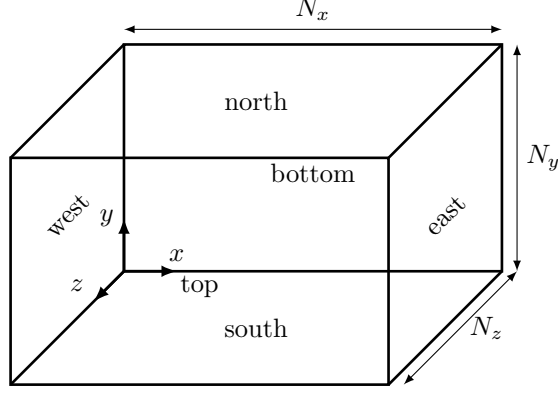


Figure 1: Schematic of the computational domain. We denote the axis directions .

3.2. High-order Godunov-type finite-volume formulation

In this section, we detail the spatial discretization of the convective (inviscid) fluxes and the diffusive (viscid) fluxes. The semi-discrete form of the governing equations (1) for the cell-averaged state $\bar{\mathbf{U}}_{i,j,k}$ in cell (i, j, k) is given by

$$\begin{aligned}
\frac{d}{dt} \bar{\mathbf{U}}_{i,j,k} = & -\frac{1}{\Delta x_{i,j,k}} \left[\left(\mathbf{F}_{i+\frac{1}{2},j,k}^c - \mathbf{F}_{i+\frac{1}{2},j,k}^d \right) - \left(\mathbf{F}_{i-\frac{1}{2},j,k}^c - \mathbf{F}_{i-\frac{1}{2},j,k}^d \right) \right] \\
& -\frac{1}{\Delta y_{i,j,k}} \left[\left(\mathbf{G}_{i,j+\frac{1}{2},k}^c - \mathbf{G}_{i,j+\frac{1}{2},k}^d \right) - \left(\mathbf{G}_{i,j-\frac{1}{2},k}^c - \mathbf{G}_{i,j-\frac{1}{2},k}^d \right) \right] \\
& -\frac{1}{\Delta z_{i,j,k}} \left[\left(\mathbf{H}_{i,j,k+\frac{1}{2}}^c - \mathbf{H}_{i,j,k+\frac{1}{2}}^d \right) - \left(\mathbf{H}_{i,j,k-\frac{1}{2}}^c - \mathbf{H}_{i,j,k-\frac{1}{2}}^d \right) \right] \\
& + \bar{\mathbf{S}}_{i,j,k} = \mathcal{R}_{\text{NSE}}
\end{aligned} \tag{18}$$

The convective fluxes are calculated using a high-order shock-capturing scheme in combination with the HLLC approximate Riemann solver. Figure 2 shows a schematic of reconstruction and flux calculation. We summarize the procedure step-by-step exemplarily for the flux $\mathbf{F}_{i+\frac{1}{2},j,k}^c$, i.e., the convective flux in x -direction at the cell face $x_{i+\frac{1}{2},j,k}$. The procedure is applied dimension-by-dimension (method of lines), and the calculation of \mathbf{G}^c and \mathbf{H}^c in y - and z -directions is analogous. To improve legibility, we drop the indices j and k for y - and z -directions, respectively, for the remainder of this section. We provide more details in Appendix C.

1. We approximate the matrix of right eigenvectors \mathbf{K} of the Jacobian $\mathbf{A}(\mathbf{W}) = (\partial \mathbf{U} / \partial \mathbf{W})^{-1} \partial \mathbf{F}^c / \partial \mathbf{W}$ at the cell face $x_{i+\frac{1}{2}}$, see Appendix C.1. The matrix of right eigenvectors is evaluated for the frozen state $\mathbf{W}_{i+\frac{1}{2}}$, i.e., $\mathbf{K}_{i+\frac{1}{2}} = \mathbf{K}_{i+\frac{1}{2}}(\mathbf{W}_{i+\frac{1}{2}})$. Typically, we use an arithmetic average of the neighboring cell center values \mathbf{W}_i and \mathbf{W}_{i+1} to compute $\mathbf{W}_{i+\frac{1}{2}}$. Roe averaging is also possible.
2. The matrix of left eigenvectors $\mathbf{K}_{i+\frac{1}{2}}^{-1}$ computed at the cell face $x_{i+\frac{1}{2}}$ is then used to project the primitive variables in a given reconstruction stencil (see next step) into characteristic space.

$$\tilde{\mathbf{W}}_i = \mathbf{K}_{i+\frac{1}{2}}^{-1} \mathbf{W}_i \tag{19}$$

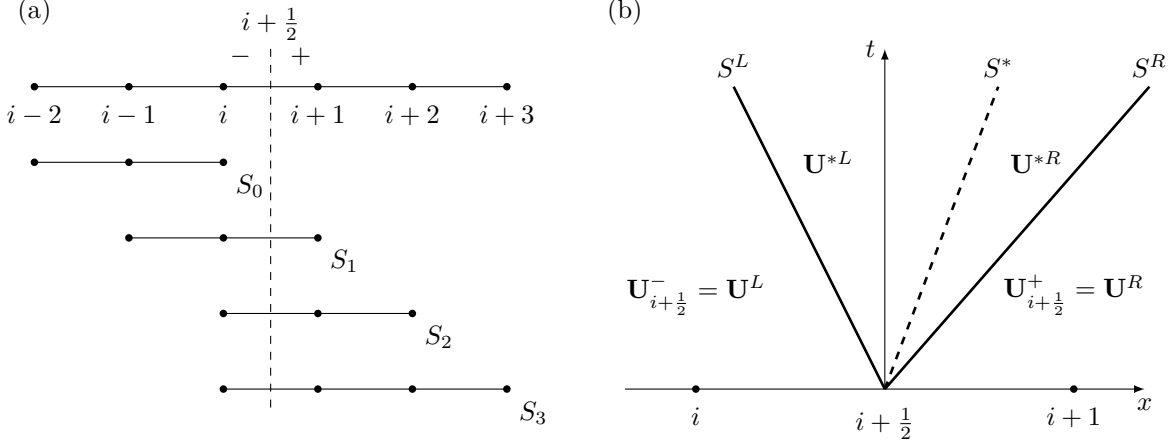


Figure 2: (a) Schematic of the spatial reconstruction and (b) schematic of the HLLC approximate solution to the resulting Riemann problem. (a): The stencils S_k corresponding to the interpolants $p_{k,i+\frac{1}{2}}^-$ for WENO5-Z and TENO6-A reconstruction are shown. (b): The corresponding Riemann problem is solved by the HLLC Riemann solver. The emanating wave structure (s^L, s^*, s^R) and the resulting intermediate start states \mathbf{U}^{*L} and \mathbf{U}^{*R} are visualized.

3. We then apply WENO and TENO shock-capturing schemes for cell face reconstruction in characteristic space. In particular, the reconstruction procedure is applied independently for each component of the vector of characteristic variables. Given the cell-averaged values \bar{v}_i of a function $v(x)$ within a K -point global stencil $S^K = \bigcup_{k=0}^{r-1} S_k$, WENO/TENO schemes assemble the reconstructed cell face value as a solution-adaptive convex combination of Harten-type interpolation polynomials on candidate sub-stencils S_k . Figure 2 shows a schematic of the reconstruction stencils for the cell face at $x_{i+\frac{1}{2}}$. The interpolated cell face values from the left and from the right $v_{i+\frac{1}{2}}^\mp$ are obtained as

$$v_{i+\frac{1}{2}}^\mp = \sum_{k=0}^{r-1} \omega_{k,i+\frac{1}{2}}^\mp p_{k,i+\frac{1}{2}}^\mp, \quad p_{k,i+\frac{1}{2}}^\mp = \sum_{l=0}^{r_k-1} c_{k,l}^\mp \bar{v}_{i-k+l}, \quad (20)$$

where $p_{k,i+\frac{1}{2}}^\mp$ are the interpolation polynomials evaluated at $x_{i+\frac{1}{2}}$ and $\omega_{k,i+\frac{1}{2}}^\mp$ are the corresponding nonlinear solution-adaptive weights. In this work, we use WENO5-Z [33] and TENO6-A [34] schemes. For WENO5-Z $S^5 = \{S_0, S_1, S_2\}$ and $r_k = \{3, 3, 3\}$, and for TENO6-A $S^6 = \{S_0, S_1, S_2, S_3\}$ and $r_k = \{3, 3, 3, 4\}$, see Fig. 2. The coefficients $c_{k,l}^\mp$ are grid-dependent, and general expressions for calculating these are given in [35]. Relations for the interpolation polynomials $p_{k,i+\frac{1}{2}}^\mp$ can be found in [36, 35, 33, 34], and definitions for the nonlinear weights $\omega_{k,i+\frac{1}{2}}^\mp$ for the WENO5-Z and TENO6-A schemes are given in [33] and [34], respectively.

4. The cell face reconstructed values are projected back into physical space by $\mathbf{W}_{i+\frac{1}{2}}^\mp = \mathbf{K}_{i+\frac{1}{2}} \tilde{\mathbf{W}}_{i+\frac{1}{2}}^\mp$, and the corresponding conservative states are calculated $\mathbf{U}_{i+\frac{1}{2}}^\mp = \mathcal{L} \mathbf{w}_{i+\frac{1}{2}}^\mp$.
5. When the five-equation diffuse-interface model is used, we combine the aforementioned shock-

capturing methods with a THINC-type interface-capturing method [37, 38, 39]. THINC prevents excessive smearing of the interface. THINC reconstruction is used only in interface cells, i.e., cells with $\epsilon_\alpha \leq \alpha_{1,i} \leq 1 - \epsilon_\alpha$ and $(\alpha_{1,i+1} - \alpha_{1,i})(\alpha_{1,i} - \alpha_{1,i-1}) > 0$. We use $\epsilon_\alpha = 10^{-4}$ in this work. In cells away from the interface, we still resort to shock-capturing methods. For a given cell (i), THINC assumes the volume fraction field to follow a locally fitted tangent hyperbolic profile

$$\alpha_{1,i}^{THINC}(x) = \frac{1}{2} \left[1 + \tanh \left(\beta_i \left(\frac{x - x_{i-\frac{1}{2}}}{\Delta x_i} + x_{c,i} \right) \right) \right], \quad x \in \left[x_{i-\frac{1}{2}}, x_{i+\frac{1}{2}} \right], \quad (21)$$

where the parameter $\beta_i = \beta |n_{x,i}| + 0.01$ determines the interface thickness in the direction of reconstruction (here x -direction) [38]. $n_{x,i}$ is the corresponding component of the interface normal \mathbf{n} , and $x_{c,i}$ gives the location of the center of the interface. We choose $\beta = 1.0$. The interpolated cell face values from the left and from the right are

$$\alpha_{1,i+\frac{1}{2}}^{THINC,-} = \frac{1}{2} [1 + \tanh(\beta_i(1 + x_{c,i}))], \quad (22)$$

$$\alpha_{1,i+\frac{1}{2}}^{THINC,+} = \frac{1}{2} [1 + \tanh(\beta_{i+1}x_{c,i+1})]. \quad (23)$$

The reconstructed phase densities $(\alpha_1 \rho_1)_{i+\frac{1}{2}}^\mp$ and $(\alpha_2 \rho_2)_{i+\frac{1}{2}}^\mp$ are adapted consistently, see [40]. In the present implementation, velocities and pressure are not affected by the THINC routine and are still reconstructed by shock-capturing schemes.

6. The local Riemann problem at the cell face $x_{i+\frac{1}{2}}$ is approximately solved by the HLLC Riemann solver [41, 42], $\mathbf{F}_{i+\frac{1}{2}}^c = \mathbf{F}^{\text{HLLC}}(\mathbf{U}_{i+\frac{1}{2}}^-, \mathbf{U}_{i+\frac{1}{2}}^+)$, where the two-argument function $\mathbf{F}^{\text{HLLC}}(\mathbf{U}^L, \mathbf{U}^R)$ is the numerical flux associated with the HLLC solver. States and fluxes left and right of the cell face are denoted by the superscript $K = L, R$. The HLLC flux is

$$\begin{aligned} \mathbf{F}^{\text{HLLC}} &= \frac{1 + \text{sign}(s^*)}{2} (\mathbf{F}^L + s^- (\mathbf{U}^{*L} - \mathbf{U}^L)) \\ &+ \frac{1 - \text{sign}(s^*)}{2} (\mathbf{F}^R + s^+ (\mathbf{U}^{*R} - \mathbf{U}^R)), \end{aligned} \quad (24)$$

where $\mathbf{F}^K = \mathbf{F}^c(\mathbf{U}^K)$, and \mathbf{U}^{*K} is the intermediate star state given by

$$\mathbf{U}^{*K} = \left(\frac{s^K - u^K}{s^K - s^*} \right) \begin{bmatrix} \rho^K \\ \rho^K s^* \\ \rho^K v^K \\ \rho^K w^K \\ E^K + (s^* - u^K) \left(\rho^K s^* + \frac{p^K}{s^K - u^K} \right) \end{bmatrix} \quad (25)$$

for the single-phase Riemann problem and by

$$\mathbf{U}^{*K} = \left(\frac{s^K - u^K}{s^K - s^*} \right) \begin{bmatrix} (\alpha_1 \rho_1)^K \\ (\alpha_2 \rho_2)^K \\ \rho^K s^* \\ \rho^K v^K \\ \rho^K w^K \\ E^K + (s^* - u^K) \left(\rho^K s^* + \frac{p^K}{s^K - u^K} \right) \\ \alpha_1^K \end{bmatrix} \quad (26)$$

for the two-phase diffuse-interface Riemann problem, respectively. The relations for the wave speeds $(s^-, s^+, s^L, s^K, s^*)$ are given in Appendix C.2. Following [29, 20], the normal component of the velocity at the cell face is consistently upwinded according to

$$u_{i+\frac{1}{2}}^{\text{HLLC}} = \frac{1 + \text{sign}(s^*)}{2} \left[u^L + s^- \left(\frac{s^L - u^L}{s^L - s^*} - 1 \right) \right] + \frac{1 - \text{sign}(s^*)}{2} \left[u^R + s^+ \left(\frac{s^R - u^R}{s^R - s^*} - 1 \right) \right], \quad (27)$$

The diffusive fluxes $\mathbf{F}_{i\pm\frac{1}{2},j,k}^d$, $\mathbf{G}_{i,j\pm\frac{1}{2},k}^d$, and $\mathbf{H}_{i,j,k\pm\frac{1}{2}}^d$ are calculated via central finite differences, see Sec. 3.4 in [12] for more details regarding the implementation and Appendix A for an overview on available finite-difference stencils.

3.3. Positivity-preserving scheme

Negative or zero values for density or internal energy are non-physical. Additionally, in the DIM, negative phase densities are non-physical, and the volume fraction has to be bounded between zero

and one. States which fulfill these requirements are said to be physically admissible. For the stiffened gas EOS, positive internal energy corresponds to a positive squared speed of sound, see Eq. (12). The squared speed of sound can conveniently be evaluated by the helper variable $\rho c^2 = \gamma(p + p_\infty)$. Therefore, we can say that a given flow state is physically admissible if

$$\text{Single-phase \& SIM: } \{ \mathbf{W} | \rho > 0, \rho c^2 > 0 \}, \quad (28)$$

$$\text{DIM: } \{ \mathbf{W} | 0 \leq \alpha_1 \leq 1, \alpha_1 \rho_1 > 0, \alpha_2 \rho_2 > 0, \rho c^2 > 0 \}. \quad (29)$$

In general, high-order shock-capturing schemes and corresponding high-order HLLC fluxes (see Sec. 3.2) are not positivity-preserving and may produce physically non-admissible states. To this end, we use interpolation and flux limiters [43, 21] to ensure physically admissible states at all times during the simulation. The positivity-preserving scheme consists of two successive limiters which we briefly outline below. We refer to [43, 21] for more details.

1. Interpolation limiter (IL): First-order (FO) spatial reconstruction, i.e., $\mathbf{U}_{i+\frac{1}{2}}^{-,\text{FO}} = \mathbf{U}_i$ and $\mathbf{U}_{i+\frac{1}{2}}^{+,\text{FO}} = \mathbf{U}_{i+1}$, yields physically admissible reconstructed states given physically admissible cell center values \mathbf{U}_i and \mathbf{U}_{i+1} . Therefore, we can limit the high-order reconstruction, i.e., WENO/TENO reconstruction (+ THINC for DIM), by locally switching to first-order reconstruction. For single-phase and sharp-interface simulations, the interpolation limiting process consists of two independent loops. Firstly, we check whether the reconstructed density violates positivity. If the reconstructed density at a given cell face violates the user-specified tolerance, i.e., $\rho_{i+\frac{1}{2}}^- < \epsilon_\rho$, the interpolation limiter is activated, $\delta_{i+\frac{1}{2}}^{\text{IL},-} = 1$, and we locally switch from high-order to first-order reconstruction. Otherwise, $\delta_{i+\frac{1}{2}}^{\text{IL},-} = 0$.

$$\mathbf{U}_{i+\frac{1}{2}}^- = \left(1 - \delta_{i+\frac{1}{2}}^{\text{IL},-} \right) \mathbf{U}_{i+\frac{1}{2}}^- + \delta_{i+\frac{1}{2}}^{\text{IL},-} \mathbf{U}_{i+\frac{1}{2}}^{-,\text{FO}} \quad (30)$$

Secondly, this process is repeated for the squared speed of sound with the corresponding tolerance $\epsilon_{\rho c^2}$. In the DIM, the limiting process consists of three independent loops over partial densities $\rho_i \alpha_i$ (with ϵ_ρ), volume fraction α_1 (with ϵ_α), and squared speed of sound (with $\epsilon_{\rho c^2}$), respectively. We obtain physically admissible reconstructed states $\mathbf{U}_{i+\frac{1}{2}}^-$ and $\mathbf{W}_{i+\frac{1}{2}}^-$, respectively.

2. Flux limiter (FL): The first-order HLLC flux $\mathbf{F}_{i+\frac{1}{2}}^{\text{HLLC}, \text{FO}} = \mathbf{F}^{\text{HLLC}}(\mathbf{U}_i, \mathbf{U}_{i+1})$ is positivity- and boundedness-preserving (e.g., [21]). We use the high-order HLLC flux and perform pseudo-time integration. Should the resulting state after integration in pseudo-time violate positivity (or boundedness), we can limit the high-order HLLC flux by locally switching to the first-order HLLC flux. Similarly to the interpolation limiter, for single-phase and sharp-interface simulations, the flux limiting process consists of independent loops over density and squared speed of sound. First, we conduct the flux limiting procedure for the density. Should the density after pseudo-

time integration violate the positivity threshold ϵ_ρ , we activate the flux limiter, $\delta_{i+\frac{1}{2}}^{\text{FL}} = 1$, and we limit the flux. Otherwise, $\delta_{i+\frac{1}{2}}^{\text{FL}} = 0$.

$$\mathbf{F}_{i+\frac{1}{2}}^{\text{HLLC}} = \left(1 - \delta_{i+\frac{1}{2}}^{\text{FL}}\right) \mathbf{F}_{i+\frac{1}{2}}^{\text{HLLC}} + \delta_{i+\frac{1}{2}}^{\text{FL}} \mathbf{F}_{i+\frac{1}{2}}^{\text{HLLC,FO}} \quad (31)$$

Second, this process is repeated for the squared speed of sound with $\epsilon_{\rho c^2}$. In the DIM, the flux limiting process consists of independent loops over partial densities (with ϵ_ρ), volume fraction (with ϵ_α), and squared speed of sound (with $\epsilon_{\rho c^2}$). Here, the upwinded normal velocities u^{HLLC} are limited consistently. Finally, we obtain a positivity limited flux which we use for time integration.

Contrary to [43, 21], we do not blend high-order and first-order interpolations/fluxes, but instead we use a binary switch $\delta_{i+\frac{1}{2}}^{\text{IL/FL}}$. This simplifies implementation and, in our tests, does not influence solution accuracy. If multistep Runge-Kutta time integration schemes are used, the limiting procedure is applied at every sub-step. By default, we activate positivity-preserving limiters for all two-phase calculations. For single-precision calculations, we set the tolerances as $\epsilon_\rho = 10^{-10}$, $\epsilon_{\rho c^2} = 10^{-8}$, $\epsilon_\alpha = 10^{-10}$, and we choose $\epsilon_\rho = 10^{-12}$, $\epsilon_{\rho c^2} = 10^{-10}$, $\epsilon_\alpha = 10^{-12}$ for double-precision calculations.

3.4. Temporal integration

The semi-discrete system of equations is integrated in time according to

$$\mathbf{U}^{n+1} = \mathcal{I}(\mathbf{U}^n, \mathcal{R}_{\text{NSE}}(\mathbf{U}^n), \Delta t^n), \quad (32)$$

where the operator $\mathcal{I}(\cdot)$ denotes an explicit time-integration scheme. The time step and time step size are denoted by the superscript n and by Δt , respectively. A common choice is the third-order total variation diminishing Runge-Kutta scheme \mathcal{I}_{RK3} [44]

$$\mathbf{U}^{(1)} = \mathbf{U}^n + \Delta t \mathcal{R}_{\text{NSE}}(\mathbf{U}^n), \quad (33)$$

$$\mathbf{U}^{(2)} = \frac{3}{4} \mathbf{U}^n + \frac{1}{4} \mathbf{U}^{(1)} + \frac{1}{4} \Delta t \mathcal{R}_{\text{NSE}}(\mathbf{U}^{(1)}), \quad (34)$$

$$\mathbf{U}^{n+1} = \frac{1}{3} \mathbf{U}^n + \frac{2}{3} \mathbf{U}^{(2)} + \frac{2}{3} \Delta t \mathcal{R}_{\text{NSE}}(\mathbf{U}^{(2)}). \quad (35)$$

We compute the time step size Δt according to a CFL criterion accounting for inviscid and viscous contributions, as detailed in [17]. Table A.10 gives an overview on time integration schemes implemented in JAX-Fluids.

3.5. Single-phase model (SPM)

The solution of the single-phase equations is straightforward. The steps outlined in the previous Sec. 3.2 can be executed with the appropriate definitions of state and flux vectors given in Sec. 2.1.

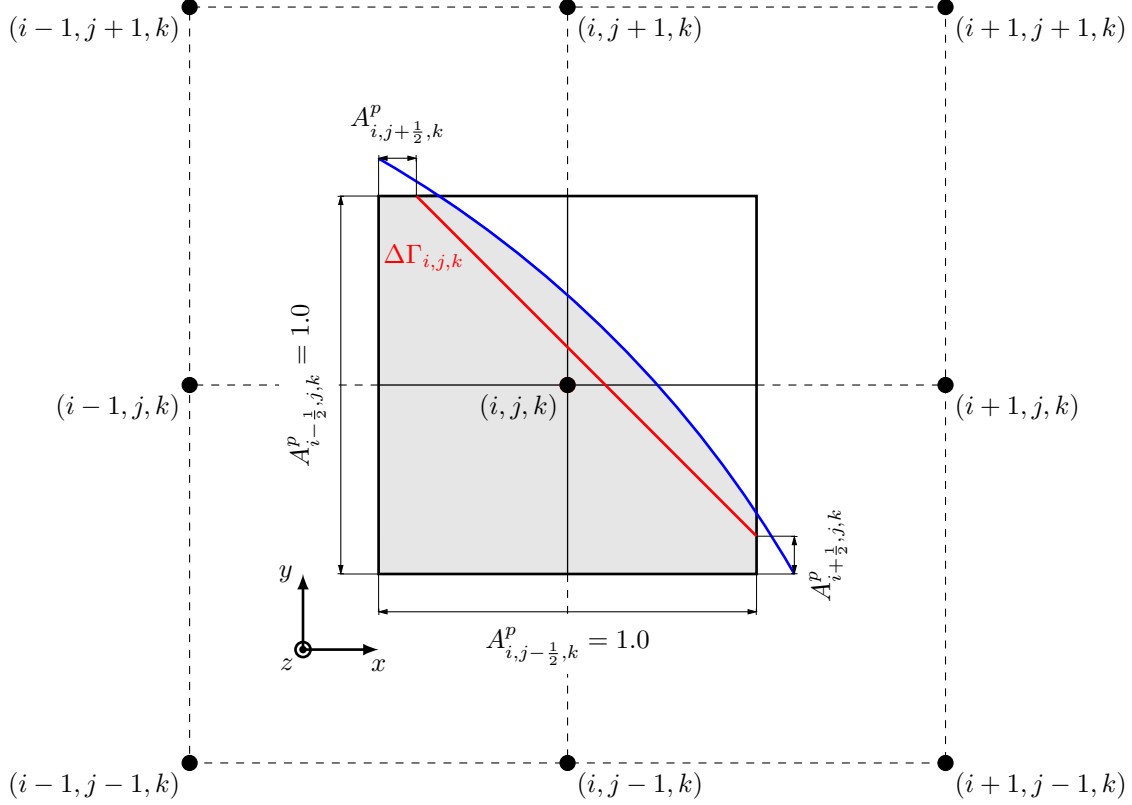


Figure 3: Schematic finite-volume discretization for cut cell (i, j, k) on a Cartesian grid. The black dots represent the cell centers. The blue line indicates the interface, and the red line depicts the linear approximation of the interface. The figure illustrates a two-dimensional slice in the (x, y) -plane. (For interpretation of the references to color in this figure legend, the reader is referred to the web version of this article.)

3.6. Level-set model (LSM)

In the level-set method [15, 16], two distinct phases are separated by a sharp interface. We track the interface implicitly by a scalar function $\phi(\mathbf{x}, t)$ that satisfies the signed distance property $|\nabla\phi| = 1$. The zero level-set describes the interface location

$$\Gamma(\mathbf{x}, t) = \{\mathbf{x} \mid \phi(\mathbf{x}, t) = 0\}. \quad (36)$$

The distinction between the two phases $p \in \{1, 2\}$ is given by the sign of the level-set. Figure 3 shows a finite-volume cell (i, j, k) that contains an interface segment Γ . We refer to such cells as *cut cells*. Cells that do not contain an interface segment are referred to as *full cells*. The gray region in the figure indicates the volumetric portion $\alpha_{i,j,k}^p$ of the cell that is occupied by phase p (not to be confused with $\alpha_{1,i,j,k}$ which is the volume fraction of fluid/phase 1 in the diffuse-interface method). We define apertures $A_{i\pm\frac{1}{2},j,k}^p$, $A_{i,j\pm\frac{1}{2},k}^p$, and $A_{i,j,k\pm\frac{1}{2}}^p$ as the cell face fractions that are covered by phase p .

In the LSM, we solve the Navier-Stokes equations (Eq. (18)) for both phases separately. For full

cells, Eq. (18) remains unchanged. For cut cells, the following modification to the equation is made.

$$\begin{aligned}
\frac{d}{dt} \alpha_{i,j,k}^p \bar{\mathbf{U}}_{i,j,k}^p = & -\frac{1}{\Delta x} \left[A_{i+\frac{1}{2},j,k}^p \left(\mathbf{F}_{i+\frac{1}{2},j,k}^{c,p} - \mathbf{F}_{i+\frac{1}{2},j,k}^{d,p} \right) - A_{i-\frac{1}{2},j,k}^p \left(\mathbf{F}_{i-\frac{1}{2},j,k}^{c,p} - \mathbf{F}_{i-\frac{1}{2},j,k}^{d,p} \right) \right] \\
& -\frac{1}{\Delta y} \left[A_{i,j+\frac{1}{2},k}^p \left(\mathbf{G}_{i,j+\frac{1}{2},k}^{c,p} - \mathbf{G}_{i,j+\frac{1}{2},k}^{d,p} \right) - A_{i,j-\frac{1}{2},k}^p \left(\mathbf{G}_{i,j-\frac{1}{2},k}^{c,p} - \mathbf{G}_{i,j-\frac{1}{2},k}^{d,p} \right) \right] \\
& -\frac{1}{\Delta z} \left[A_{i,j,k+\frac{1}{2}}^p \left(\mathbf{H}_{i,j,k+\frac{1}{2}}^{c,p} - \mathbf{H}_{i,j,k+\frac{1}{2}}^{d,p} \right) - A_{i,j,k-\frac{1}{2}}^p \left(\mathbf{H}_{i,j,k-\frac{1}{2}}^{c,p} - \mathbf{H}_{i,j,k-\frac{1}{2}}^{d,p} \right) \right] \quad (37) \\
& + \alpha_{i,j,k} \bar{\mathbf{S}}_{i,j,k} \\
& - \frac{1}{\Delta x \Delta y \Delta z} \left[\mathbf{X}_{i,j,k}^{c,p} + \mathbf{X}_{i,j,k}^{d,p} \right] = \mathcal{R}_{\text{NSE}}
\end{aligned}$$

Here, we weigh the cell-average state $\bar{\mathbf{U}}_{i,j,k}^p$ and cell face fluxes $\mathbf{F}_{\dots}^{c,p}$, $\mathbf{F}_{\dots}^{d,p}$, $\mathbf{G}_{\dots}^{c,p}$, $\mathbf{G}_{\dots}^{d,p}$, $\mathbf{H}_{\dots}^{c,p}$, $\mathbf{H}_{\dots}^{d,p}$ with the volume fraction $\alpha_{i,j,k}^p$ and the corresponding apertures A_{\dots}^p , respectively. The terms $\mathbf{X}^{c,p}$ and $\mathbf{X}^{d,p}$ denote the convective and dissipative interface fluxes. They read

$$\mathbf{X}^{c,p} = \begin{bmatrix} 0 \\ p_{\Gamma} \Delta \Gamma^p \\ p_{\Gamma} \Delta \Gamma^p \cdot \mathbf{u}_{\Gamma} \end{bmatrix}, \quad \mathbf{X}^{d,p} = \begin{bmatrix} 0 \\ \tau_{\Gamma}^T \Delta \Gamma^p \\ (\tau_{\Gamma}^T \Delta \Gamma^p) \cdot \mathbf{u}_{\Gamma} \end{bmatrix}. \quad (38)$$

Here, p_{Γ} and \mathbf{u}_{Γ} denote the interface pressure and interface velocity, respectively, and are obtained by solving a two-material Riemann problem at the interface, as detailed in Appendix D.1. The projection of the interface segment reads $\Delta \Gamma^p = \Delta \Gamma \mathbf{n}_{\Gamma}^p$, where the interface normal is given by $\mathbf{n}_{\Gamma} = \mathbf{n}_{\Gamma}^1 = \nabla \phi / |\nabla \phi|$, and $\Delta \Gamma$ denotes the interface segment. Interface normals for phases 1 and 2 have opposite directions $\mathbf{n}_{\Gamma}^2 = -\mathbf{n}_{\Gamma}^1$. We compute the interface normal using fourth-order central finite-differences. Assuming a linear approximation of the level-set inside a cut cell, we analytically compute the apertures A^p , volume fraction α^p , and interface segment $\Delta \Gamma$, as described in Appendix D.2.

The level-set function is evolved by solving the level-set advection equation (6). We use high-order-upstream-central schemes [45] for the spatial discretization. The temporal integration is performed with the same scheme as used for the integration of the Navier-Stokes equations (NSE). In practice, we evolve the level-set function in a narrowband that extends over a small number of cells around the interface. It is important to note that, in the current JAX-Fluids version, the level-set algorithm requires cut cells and the narrowband to be located in a homogenous region of the computational grid, i.e., $\Delta x = \Delta y = \Delta z$.

The solution of the level-set advection equation (Eq. (6)) may violate the signed-distance property of the level-set. To recover the signed-distance property, we solve the reinitialization equation

$$\frac{\partial \phi}{\partial \tau} = -\text{sgn}(\phi^0) (|\nabla \phi| - 1) = \mathcal{R}_{\text{reinit}} \quad (39)$$

iteratively in pseudo-time τ using a fixed time step size $\Delta\tau = 0.25\Delta x$ for a fixed amount of 10 steps. Here, ϕ^0 denotes the level-set prior to reinitialization, and $\text{sgn}(\cdot)$ denotes the sign function. We discretize the spatial operators by means of third-order WENO-HJ [46] scheme. The temporal evolution is performed by the second-order Runge-Kutta scheme (see Sec. 3.4). In practice, we only reinitialize cells where the residual of Eq. (39) is above the threshold 5×10^{-2} .

The evaluation of stencils close to the interface requires reasonable cell values of the considered phase on both sides of the interface. We refer to cells that lie on the opposite side of the interface as *ghost cells* [47]. The ghost cells of one phase overlap with the real cells of the other phase. We perform a constant extrapolation in interface normal direction to populate the ghost cells with values from the real cells. The extrapolation procedure is performed on the primitive variables \mathbf{W} , and the extrapolation equation (EE) reads

$$\frac{\partial \mathbf{W}^p}{\partial \tau} = \mathbf{n}_\Gamma^p \cdot \nabla \mathbf{W} = \mathcal{R}_{\text{ext}, \mathbf{W}}. \quad (40)$$

We solve this equation iteratively in pseudo-time τ using a fixed time step size $\Delta\tau = 0.25\Delta x$ and a fixed amount of 10 steps. The right-hand side is discretized using a first-order upwind scheme. Temporal integration is performed with a single-step Euler scheme.

Quantities \mathbf{Q}_Γ that are only known at the interface, i.e., the interface velocity \mathbf{u}_Γ and interface pressure p_Γ , require extrapolation into the narrowband. We perform a two-way constant extrapolation in interface normal direction according to

$$\frac{\partial \mathbf{Q}_\Gamma}{\partial \tau} = -\text{sgn}(\phi) \mathbf{n}_\Gamma \cdot \nabla \mathbf{Q}_\Gamma = \mathcal{R}_{\text{ext}, \mathbf{Q}_\Gamma}. \quad (41)$$

We use a fixed time step size $\Delta\tau = 0.25\Delta x$ and a fixed amount of 20 steps to iteratively solve this equation. Again, first-order upwind spatial discretization and single-step Euler integration are used.

The time step size that is computed using the CFL criterion (see Sec. 3.4) based on full cells may be too large for cut cells with small volume fractions α and therefore lead to unstable integration. Furthermore, as the interface crosses cell faces, cells are vanishing and new cells are created. This process must be accounted for to prevent numerical instability. We employ a conservative mixing procedure [48, 49] that treats both of these issues (see Appendix D.3).

We detail the implementation of the algorithm in Figure 6. For further insight on the presented level-set method, the reader is referred to the implementation of Hoppe et al. [17].

Notation	Description	Details
\mathcal{I}	Explicit time-integration	Section 3.4
\mathcal{L}	Transformation between primitive and conservative variables	Section 2
\mathcal{R}_{NSE}	Right-hand side computation of the NSE	Section 3.2
\mathcal{R}_{LSA}	Right-hand side computation of the LSA	Section 3.6
$\mathcal{R}_{\text{ext},\mathbf{W}}$	Right-hand side computation of the EE for primitives	Section 3.6
$\mathcal{R}_{\text{ext},\mathbf{Q}_\Gamma}$	Right-hand side computation of the EE for interface quantities	Section 3.6
$\mathcal{H}_F, \mathcal{H}_E, \mathcal{H}_V$	Face, edge, and vertex halo updates, respectively	Section 4.3
\mathcal{M}	Mixing procedure	Appendix D.3
\mathcal{Q}_Γ	Interface quantity computation	Appendix D.1

Table 1: Notation and description of relevant operators/functions that are executed within a single Runge-Kutta stage of JAX-Fluids.

3.7. Diffuse-interface model (DIM)

For the five-equation diffuse-interface model, Eq. (18) is solved with the state and flux vectors defined in Sec. 2.3. Following [29], the source term in the advection equation (see Eq. (9)),

$$\frac{\partial \alpha_1}{\partial t} + \nabla \cdot (\alpha_1 \mathbf{u}) = \alpha_1 \nabla \cdot \mathbf{u},$$

is discretized consistently with the convective flux calculation

$$(\alpha_1 \nabla \cdot \mathbf{u})_{i,j,k} = \alpha_{1,i,j,k} \left[\frac{u_{i+1/2,j,k}^{\text{HLLC}} - u_{i-1/2,j,k}^{\text{HLLC}}}{\Delta x_{i,j,k}} + \frac{v_{i,j+1/2,k}^{\text{HLLC}} - v_{i,j-1/2,k}^{\text{HLLC}}}{\Delta y_{i,j,k}} + \frac{w_{i,j,k+1/2}^{\text{HLLC}} - w_{i,j,k-1/2}^{\text{HLLC}}}{\Delta z_{i,j,k}} \right], \quad (42)$$

where the velocities used are the ones upwinded by the Riemann solver, see Sec. 3.2.

The THINC reconstruction procedure requires the calculation of the interface normal $\mathbf{n}_{i,j,k}$, see Sec. 3.2. The interface normal $\mathbf{n}_{i,j,k}$ is computed from a smoothed volume fraction field ψ ,

$$\psi_{i,j,k} = \frac{\alpha_{1,i,j,k}^{0.1}}{\alpha_{1,i,j,k}^{0.1} + (1 - \alpha_{1,i,j,k})^{0.1}}, \quad (43)$$

according to

$$\mathbf{n}_{i,j,k} = \frac{(\nabla \psi)_{i,j,k}}{|(\nabla \psi)_{i,j,k}|}, \quad (44)$$

where we use second-order central differences to evaluate the spatial derivatives.

Notation	Description
\mathbf{U}	Conservative variables
\mathbf{W}	Primitive variables
ϕ	Level-set
\mathbf{Q}_Γ	Interface quantities

Table 2: Notation and description of relevant buffers.

4. Parallelization strategy

4.1. JAX-specific aspects

Requirements for the parallelization of the JAX-Fluids CFD code are high-performance and differentiability. Although there are third-party packages to parallelize JAX code, e.g., `mpi4jax` [50], we use JAX inherent tools to implement our parallelization strategy. This ensures that differentiability is maintained while optimal performance is achieved. In particular, we use `jax.pmap`, which expresses single-program multiple-data code, to transform the compute-intensive functions. Similarly to `jax.jit`, `jax.pmap` will compile the function with the XLA (Accelerated Linear Algebra) (e.g., [13]) compiler and subsequently execute the function in parallel on the specified devices. Furthermore, we use `jax.lax.ppermute` to perform collective permutations of data between devices. `jax.lax.ppermute` requires each device to send data to and receive data from exactly one other device.

4.2. Homogeneous domain decomposition

For single device simulations, the computational domain in JAX-Fluids has the shape $[N_x + 2N_h, N_y + 2N_h, N_z + 2N_h]$, where N_i , $i \in x, y, z$ represents the number of cells in the spatial directions. N_h is the number of halo cells. We decompose the computational domain into a $S_x \times S_y \times S_z$ grid of equally sized blocks. Here, S_i , $i \in x, y, z$ represents the number of blocks in the spatial directions. A single block has the shape $[N_x/S_x + 2N_h, N_y/S_y + 2N_h, N_z/S_z + 2N_h]$. For multi-device simulations, the shape of the entire computational domain becomes $[S_T, N_x/S_x + 2N_h, N_y/S_y + 2N_h, N_z/S_z + 2N_h]$, where the leading array axis has length $S_T = S_x S_y S_z$. Figure 4 shows an exemplary domain decomposition with four blocks arranged in a $2 \times 2 \times 1$ grid (halo cells are not shown). The transformation `jax.pmap` maps a function over the leading array axis S_T , generating a replication of the function on each XLA device, and subsequently executing it in parallel. By *XLA device* one generally refers to any computational device that can be targeted by the XLA compiler. In this work, we use the term XLA device synonymously with GPUs and TPUs.

4.3. Halo update algorithm

Neighboring blocks in the decomposed domain must communicate data to update their halo cells. Figure 5 illustrates a schematic of two neighboring blocks in x -direction, namely block 1 and block 2.

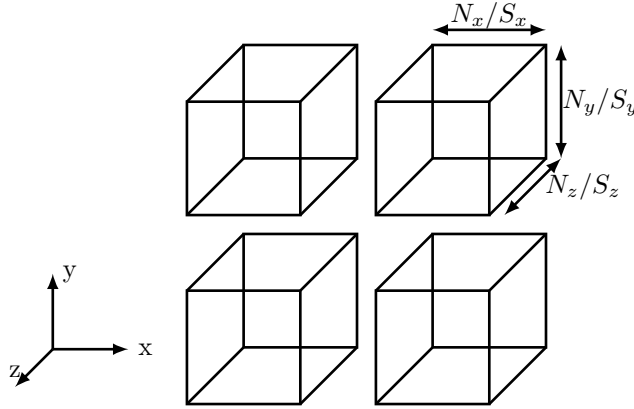


Figure 4: Exemplary domain decomposition with four blocks arranged in a $2 \times 2 \times 1$ grid.

We generally distinguish between internal cells and halo cells. Furthermore, we define three halo cell regions, i.e., face, edge, and vertex halo cells. In Fig. 5, we schematically show the halo update of block 1, i.e., block 1 is receiving and block 2 is sending data. For the sake of clarity, we only show halo cells that are located at the east side of block 1. The corresponding cells in block 2, that are required for the halo update, are highlighted accordingly. The figure shows that

- face halo cells of the receiving block correspond to internal cells of the sending block.
- edge halo cells of the receiving block correspond to face halo cells of the sending block.
- vertex halo cells of the receiving block correspond to edge halo cells of the sending block.

This means that we must first update face, then edge, and lastly vertex halos. During each of these updates, we iterate over (a subset of) the axis directions $\in \{east, west, north, south, top, bottom\}$. The axis direction indicates the location of the halo cells that shall be updated. We perform a collective permutation with `jax.lax.ppermute` in the opposite direction of the indicated axis direction to receive the required data from neighboring blocks. In particular, we do the following:

1. **Face halo update:** We iterate over all axis directions and update the face halo cells located at the present side of the block.
2. **Edge halo update:** We iterate over the axis directions $\in \{east, west, north, south\}$. During the *east* and *west* iterations, we update all edge halo cells at the present side of the block. During the *north* and *south* directions, the remaining edge halo cells are updated, preventing duplicate updates.
3. **Vertex halo update:** We iterate over the axis directions $\in \{east, west\}$ and update the vertex halo cells located at the present side of the block.

During each of the aforementioned halo updates, we make the following distinction:

- **Inner halo cells:** These are halo cells, that are located at the interface of neighboring blocks. They require communication of data.

- **Outer halo cells:** These are halo cells, that are located at the outer faces of the computational domain. Here, each device updates its halos independently in accordance with the specified boundary condition. Periodic boundary conditions pose an exception. In this case, if the domain is split into multiple blocks in the periodic axis direction, nominally outer halo cells are treated like inner halo cells.

The spatial stencil structure of the utilized numerical methods dictates if halo cell regions are accessed, i.e., not all buffers require a halo update for all halo cell regions. Figure 6 illustrates the algorithm of a single Runge-Kutta stage highlighting the positions and types of halo updates. We show the algorithm for the single-phase/diffuse-interface model 1 and the level-set model 2. Table 1 and Table 2 depict the corresponding function and buffer notations. Algorithm 1 starts with given conservative and primitive variables \mathbf{U} and \mathbf{W} . We evaluate the right-hand side \mathcal{R}_{NSE} and subsequently perform a stage integration. The primitive variables are then computed from the integrated conservative variables. The stage ends with an edge halo update of \mathbf{U} and \mathbf{W} , as the spatial stencils that are used for the evaluation of \mathcal{R}_{NSE} do not access the vertex halo cells. In addition to \mathbf{U} and \mathbf{W} , algorithm 2 starts with given interface quantities \mathbf{Q}_Γ and level-set ϕ . We evaluate the right-hand sides \mathcal{R}_{NSE} and \mathcal{R}_{LSA} and perform a stage integration. In terms of halo updates, the key difference here are the extrapolation and reinitialization procedures. These constitute to a large overhead in multi-device simulations, as they require a face halo update in each iteration.

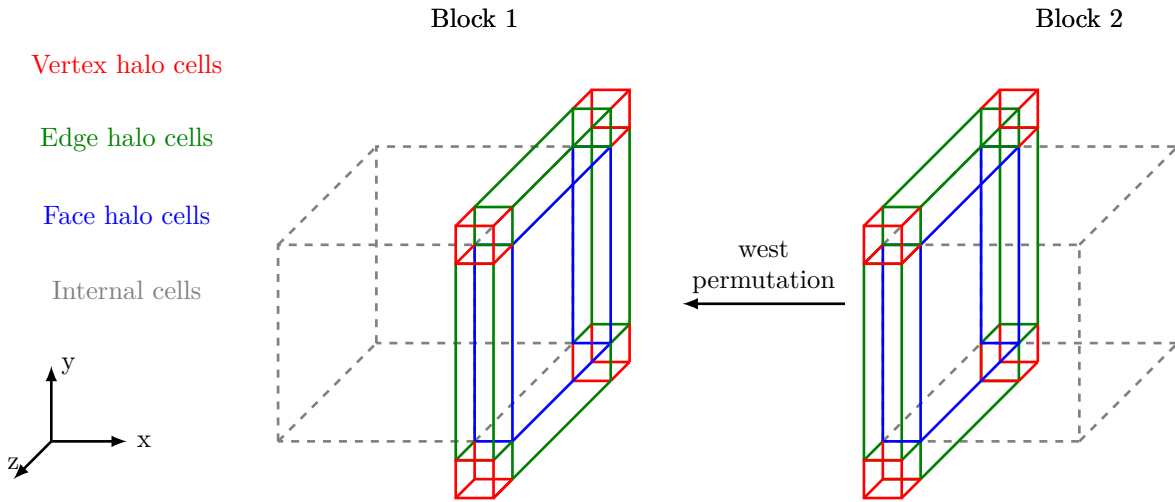


Figure 5: Schematic illustration of two adjacent blocks in x -direction within the homogeneous domain decomposition during a halo update. Depicted are the face (blue), edge (green), and vertex (red) halo cells of block 1 at the east side of the block. We highlight the corresponding cells in block 2 that are required for the halo update accordingly. This update entails a west permutation, i.e., a permutation of data from block 2 to block 1.

Algorithm 1: Single-phase and diffuse-interface model.

Data: $\mathbf{U}, \mathbf{W}, \Delta t$

$\mathbf{R}_{\text{NSE}} = \mathcal{R}_{\text{NSE}}(\mathbf{U}, \mathbf{W});$
 $\mathbf{U} = \mathcal{I}(\mathbf{U}, \mathbf{R}_{\text{NSE}}, \Delta t);$

$\mathbf{W} = \mathcal{L}_{\mathbf{U} \rightarrow \mathbf{W}}(\mathbf{U});$

$\mathbf{U}, \mathbf{W} = \mathcal{H}_{\text{E}}(\mathbf{U}, \mathbf{W});$

Algorithm 2: Level-set model.

Data: $\mathbf{U}, \mathbf{W}, \phi, \mathbf{Q}_{\Gamma}, \Delta t$

$\mathbf{R}_{\text{NSE}} = \mathcal{R}_{\text{NSE}}(\mathbf{U}, \mathbf{W}, \phi, \mathbf{Q}_{\Gamma});$
 $\mathbf{U} = \mathcal{I}(\mathbf{U}, \mathbf{R}_{\text{NSE}}, \Delta t);$

$\mathbf{R}_{\text{LSA}} = \mathcal{R}_{\text{LSA}}(\phi, \mathbf{Q}_{\Gamma});$
 $\phi = \mathcal{I}(\phi, \mathbf{R}_{\text{LSA}}, \Delta t);$

$\phi = \mathcal{H}_{\text{V}}(\phi);$
if *last RK stage* **then**
 for *reinitialization steps* **do**
 $\mathbf{R}_{\text{reinit}} = \mathcal{R}_{\text{reinit}}(\phi);$
 $\phi = \mathcal{I}(\phi, \mathbf{R}_{\text{reinit}}, \Delta t);$
 $\phi = \mathcal{H}_{\text{F}}(\phi);$
 end
 $\phi = \mathcal{H}_{\text{V}}(\phi);$
end

$\mathbf{U} = \mathcal{H}_{\text{V}}(\mathbf{U});$
 $\mathbf{U} = \mathcal{M}(\mathbf{U});$

$\mathbf{W} = \mathcal{L}_{\mathbf{U} \rightarrow \mathbf{W}}(\mathbf{U});$

$\mathbf{W} = \mathcal{H}_{\text{F}}(\mathbf{W});$
for *extrapolation steps* **do**
 $\mathbf{R}_{\text{ext}, \mathbf{W}} = \mathcal{R}_{\text{ext}, \mathbf{W}}(\mathbf{W});$
 $\mathbf{W} = \mathcal{I}(\mathbf{W}, \mathbf{R}_{\text{ext}, \mathbf{W}}, \Delta t);$
 $\mathbf{W} = \mathcal{H}_{\text{F}}(\mathbf{W});$
end

$\mathbf{U} = \mathcal{L}_{\mathbf{W} \rightarrow \mathbf{U}}(\mathbf{W});$

$\mathbf{U}, \mathbf{W} = \mathcal{H}_{\text{E}}(\mathbf{U}, \mathbf{W});$

$\mathbf{Q}_{\Gamma} = \mathcal{Q}_{\Gamma}(\mathbf{W}, \phi);$
for *extrapolation steps* **do**
 $\mathbf{R}_{\text{ext}, \mathbf{Q}_{\Gamma}} = \mathcal{R}_{\text{ext}, \mathbf{Q}_{\Gamma}}(\mathbf{Q}_{\Gamma});$
 $\mathbf{Q}_{\Gamma} = \mathcal{I}(\mathbf{Q}_{\Gamma}, \mathbf{R}_{\text{ext}, \mathbf{Q}_{\Gamma}}, \Delta t);$
 $\mathbf{Q}_{\Gamma} = \mathcal{H}_{\text{F}}(\mathbf{Q}_{\Gamma});$
end

Figure 6: Schematic algorithms for a single Runge-Kutta stage illustrating the halo updates. We compare the single-phase and diffuse-interface model (left) with the level-set model (right). The color blue highlights parts of the algorithm, which are purely level-set related. Notation and description of functions and buffers are given in Table 1 and Table 2, respectively.

5. Verification of numerical models

In this section, we present verification of the numerical models implemented in JAX-Fluids. All simulations presented in this section were performed on GPUs (either NVIDIA A6000 or NVIDIA A100) and TPUs (v3). Computations on GPUs were done exclusively with double-precision (float64), while computations on TPUs were done with single-precision (float32).

5.1. Convergence test

We perform convergence tests for the inviscid advection of a one-dimensional density profile with uniform velocity $u = 1$ and pressure $p = 1$. The material is an ideal gas with $\gamma = 1.4$. The initial density consists of two Gaussians,

$$\rho(x, t = 0) = 1 + 5 \exp(-200(x - 0.5)^2) + 5 \exp(-200(x - 1.5)^2). \quad (45)$$

We initialize cell-averaged values, i.e., for cell i the cell-averaged density reads

$$\bar{\rho}_{0_i} = \frac{1}{\Delta x_i} \int_{x_{i-1/2}}^{x_{i+1/2}} \rho(x, t = 0) dx \quad (46)$$

$$= 1 - \frac{5\sqrt{\pi}}{2\sqrt{200}\Delta x_i} \left(\left[\operatorname{erf}(\sqrt{200}(0.5 - x)) \right]_{x_{i-1/2}}^{x_{i+1/2}} + \operatorname{erf}(\sqrt{200}(1.5 - x)) \Big|_{x_{i-1/2}}^{x_{i+1/2}} \right) \quad (47)$$

The computational domain is $x \in [0, 2]$ with periodic boundary conditions on either side. The density profile is advected for one flow through time which corresponds to the final time $t = 2.0$. For the single-phase model (SPM) and level-set model (LSM), we test convergence for WENO5-Z and TENO6-A stencils. For the diffuse-interface model (DIM), we only test WENO5-Z, as the TENO6-A reconstruction occasionally introduces over- and undershoots in the volume fraction field which activate the positivity-preserving algorithm and, therefore, diminish order of convergence. We use TVD-RK3 time integration with a fixed time step size $\Delta t = 10^{-5}$ for all tests. The time step size is chosen small enough to ensure that the error due to numerical time integration does not influence the solution. In Fig. 7, we visualize the L_2 -error for successively higher spatial resolutions (from $N = 64$ to $N = 4096$ grid points). The nominal convergence order is achieved for all models.

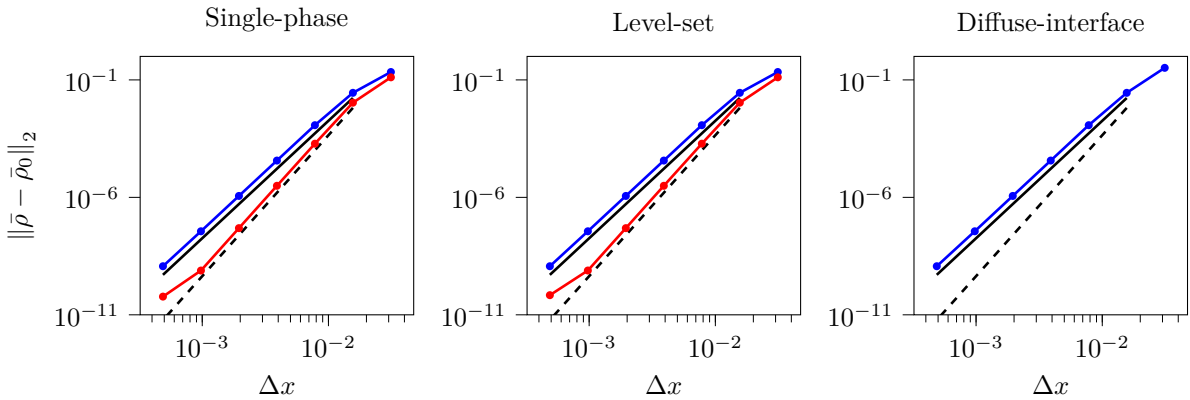


Figure 7: Error convergence for the advection of two Gaussians. For single-phase and level-set simulations WENO5-Z (—•—) and TENO6-A (—•—) reconstruction schemes were tested. For diffuse-interface simulations, WENO5-Z was tested. The solid (—) and dashed (---) black lines denote nominal convergence of $\mathcal{O}(\Delta x^5)$ and $\mathcal{O}(\Delta x^6)$, respectively.

5.2. Single-phase simulations

For single-phase simulations, we use a TENO6-A cell face reconstruction combined with an HLLC Riemann solver. The TENO6-A reconstruction is complemented by an interpolation limiter. In this work, we do not use flux limiters for single-phase simulations as the single-phase cases under investigation do not feature strong shock discontinuities. Diffusive fluxes are discretized using 6th-order central finite-difference approximations. Temporal evolution is performed with a TVD-RK3 scheme with $CFL = 0.9$.

5.2.1. Laminar boundary layer

The compressible Blasius boundary layer [51] describes the steady state two-dimensional flow over a flat plate under zero pressure gradient. We use this test case to verify the implementation of the viscous fluxes. We use an ideal gas with $\gamma = 1.4$. The computational domain $(x, y) \in [1.0, 1.5] \times [0.0, 0.4]$ is discretized using 300×200 cells with a uniform grid in x -direction and a stretched mesh in y direction. The stretching parameter is $\beta = 2.2$ (see Appendix B). The boundary conditions are a no-slip adiabatic wall at the south boundary and zero-gradient extrapolation at north and east boundaries. At the inlet (west), we impose the self-similar solution, which is computed by solving the compressible Blasius similarity equations. For the given Mach number $Ma_e = 2.25$ and Prandtl number $Pr = 0.72$, we get normalized velocity u/u_e and temperature T/T_e over the self-similar variable

$$\eta = \frac{u_e}{\sqrt{2\rho_e\mu_e u_e x}} \int_0^y \rho dy. \quad (48)$$

Here, the index e denotes free-stream conditions. To impose the Blasius solution at the inlet boundary of the domain, we numerically solve Eq. (48) for y and, subsequently, linearly interpolate the values on the grid at the boundary. The free stream unit Reynolds number is $Re = u_e \rho_e / \mu_e = 10000$. The temperature dependent dynamic viscosity is computed using the Sutherland law (see Eq. (16)) with $C = 0$, $T_{ref} = T_e$, and $\mu_{ref} = \mu_e$. We evaluate the JAX-Fluids solution at the outlet boundary $x = 1.5$ and present a comparison to the self-similar Blasius solution. Figure 8 depicts normalized velocity u/u_e and temperature T/T_e over the self-similar variable η . We achieve good agreement with the Blasius solution.

5.2.2. Turbulent channel flow

Bi-periodic turbulent channel flows serve as canonical configurations to study wall-bounded turbulence. Here, we perform direct numerical simulations (DNS) of the turbulent supersonic isothermal-wall channel flow of Coleman et al. [52, 53]. The computational domain is $(x, y, z) \in [0, 4\pi h] \times [-h, h] \times [0, 2\pi h]$. A constant mass flow rate is imposed via a uniform body force in streamwise (x) direction. The bulk density is calculated as $\rho_b = \frac{1}{2h} \int_{-h}^h \langle \rho \rangle dy$, and the bulk velocity is calculated as $U_b = \frac{1}{2h} \int_{-h}^h \langle \rho u \rangle dy$. The Mach number based on bulk velocity and speed of sound at the wall

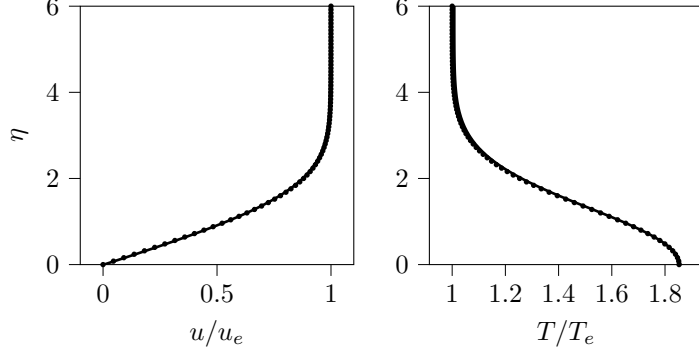


Figure 8: Compressible laminar boundary layer. Normalized velocity u/u_e and normalized temperature T/T_e profiles over the self-similar variable η . The solid lines (—) and markers (\bullet) indicate the JAX-Fluids and Blasius solution, respectively.

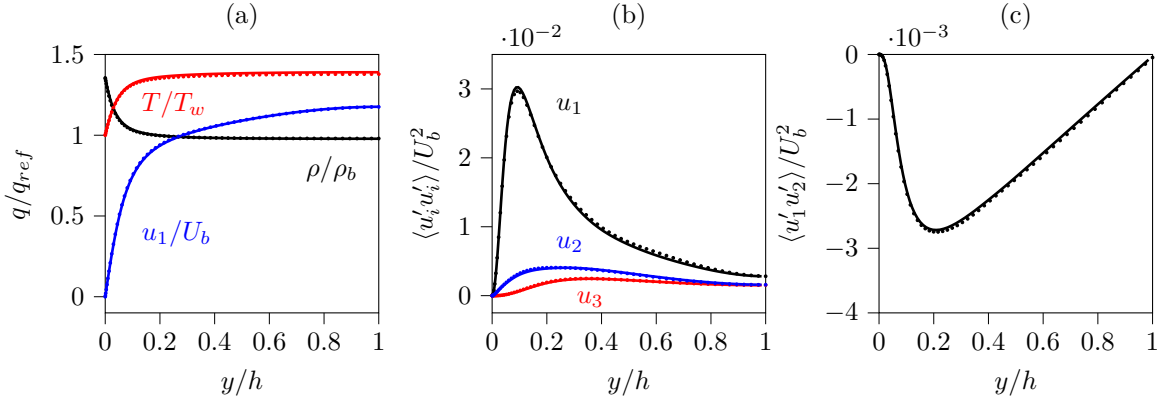


Figure 9: Statistical evaluation of the supersonic turbulent channel flow at $Ma_b = 1.5$ and $Re_b = 3000$. (a) Normalized mean profiles of density ρ/ρ_b , temperature T/T_w , and streamwise velocity u_1/U_b . (b) Normalized Reynolds normal stresses $\langle u'_i u'_i \rangle / U_b^2$. (c) Normalized Reynolds shear stress $\langle u'_1 u'_2 \rangle / U_b^2$. Reference data is taken from Coleman et al. [52]. We illustrate the JAX-Fluids solution with solid lines (—). The reference by Coleman et al. [52] is depicted with solid markers (\bullet).

$Ma_b = U_b/c_w = 1.5$. The Reynolds number based on bulk density, bulk velocity, channel half-width, and wall viscosity $Re_b = \rho_b U_b h / \mu_w = 3000$. At the channel walls isothermal, no-slip boundary conditions are imposed such that $T = 1$ and $\mathbf{u} = 0$ at $y = \pm h$. Periodic boundary conditions are applied in streamwise and spanwise direction. The fluid is assumed to be an ideal gas with constant Prandtl number $Pr = 0.7$ and constant ratio of specific heats $\gamma = 1.4$. The dynamic viscosity follows a temperature dependent power law, see Eq. (15). The computational domain is discretized by $256 \times 128 \times 128$ cells. The (DNS) grid is uniform in x - and z -direction (streamwise and spanwise direction, respectively), and a hyperbolic-tangent stretching with stretching factor $\beta = 1.8$ is applied in wall normal direction (see Appendix B for details). The first grid point is located at $y_1^+ \approx 0.34$, and the tenth point is located at $y_{10}^+ \approx 8.28$. The cell sizes in streamwise and spanwise direction are $\Delta x^+ = \Delta z^+ = 10.71$, and

the minimum and maximum cell sizes in wall normal direction are $\Delta y_{min}^+ = 0.69$ and $\Delta y_{max}^+ = 6.48$, respectively.

We run a precursor simulation of the channel flow on a coarser computational grid until a statistically steady state is reached. The simulation is initialized with a streamwise velocity that follows a laminar profile superimposed with noise along with constant pressure and density. Once a statistically steady state is obtained, we interpolate the flow field onto the aforementioned DNS grid. The DNS is run on two Nvidia A100 GPUs. Similarly to [53], we wait for 15 characteristic problem times $h/u_\tau \approx 18.38$ to let initial transients pass. We then collect 300 snapshots of the instantaneous flow field over a period of approximately $41h/u_\tau$ to compute flow statistics.

Figure 9 compares flow statistics to the DNS data of Coleman et al. [52]. We observe excellent quantitative agreement for mean flow profiles and Reynolds stresses with the cited reference. Similarly, root-mean-square fluctuations of density and temperature (not shown) are in good agreement with the reference data.

5.2.3. Turbulent boundary layer

We consider the compressible turbulent boundary layer case by Pirozzoli et al. [54]. Here, a compressible laminar boundary layer enters the domain, and transition to turbulence happens by means of blowing and suction within a small region close to the inlet boundary.

The computational domain $(x, y, z) \in [4.0, 22.0] \times [0.0, 0.5] \times [-0.0875, 0.0875]$ is discretized using $2500 \times 80 \times 380$ cells. The simulation is run on 2 Nvidia A100 GPUs. Unless mentioned otherwise, the spatial coordinates are nondimensional, with $l_{ref} = 0.00254$ m being the reference length. We impose an adiabatic no-slip wall at the south boundary and zero gradient at the outlet (east) and spanwise (top, bottom) boundaries. At the inlet (east) boundary, a self-similar Blasius solution is specified. In streamwise (x) direction, the domain is partitioned into three zones. The first zone is bound by $x \in [4, 7]$ and contains the blowing and suction region ($x_a = 4.5$ and $x_b = 5.0$). It serves as the transition region, consisting of 700 cells. The second zone is that of interest containing fully developed turbulence. It is bound by $x \in [7, 9]$ and consists of 1700 cells. Within the third zone $x \in [9, 22]$ the grid is progressively coarsened using 100 cells. This serves as a buffer region minimizing disturbances due to reflections at the outlet boundary. The grid is uniform in z -direction and a tangent stretching is applied in y -direction with $\beta = 3.5$ (see Sec. 3.1). Within the well-resolved region, the smallest grid sizes in streamwise, spanwise, and wall-normal direction are $\Delta x^+ \approx 14.2$, $\Delta z^+ \approx 5.5$, and $\Delta y^+ \approx 1.0$, respectively.

The laminar-turbulent transition is enforced by blowing and suction within a small region ($x_a \leq x \leq x_b$) close to the inlet. Here, the wall-normal component of the velocity at the wall is computed as

$$v(x, z, t) = Au_{ef}(x)g(z)h(t), \quad x_a \leq x \leq x_b, \quad (49)$$

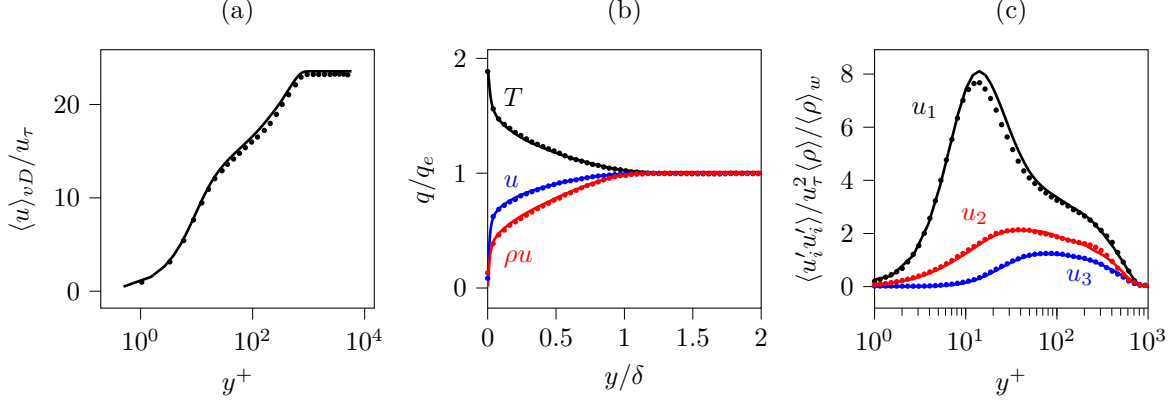


Figure 10: Statistical evaluation of the turbulent boundary layer flow at $Re_\theta = 4000$. (a) Normalized van Driest transformed velocity $\langle u \rangle_{vD}/u_\tau$ in inner scaling. (b) Normalized mean flow states $\langle T \rangle/T_e$, $\langle u \rangle/u_e$ and $\langle \rho \rangle \langle u \rangle / \rho_e u_e$ in outer scaling. (c) Normalized Reynolds normal stresses $\langle u'_i u'_i \rangle / u_\tau^2 \langle \rho \rangle / \langle \rho \rangle_w$ in inner scaling. We illustrate the JAX-Fluids solution with solid lines (—). The reference by Pirozzoli et al. [54] is depicted with markers (\bullet).

where $A = 0.04$ denotes the amplitude of the disturbance, u_e is the free stream velocity, and

$$\begin{aligned}
 f(x) &= 4 \sin \theta (1 - \cos \theta) \sqrt{27}, \\
 \theta &= 2\pi \frac{x - x_a}{x_b - x_a}, \\
 g(z) &= \sum_{l=1}^{l_{max}} Z_l \sin(2\pi l(z/L_z + \xi_l)), \\
 Z_l &= 1.25 Z_{l+1}, \quad \sum_{l=1}^{l_{max}} Z_l = 1, \\
 h(t) &= \sum_{m=1}^{m_{max}} T_m \sin(2\pi m(\beta t + \xi_m)), \\
 T_m &= 1.25 T_{m+1}, \quad \sum_{m=1}^{m_{max}} T_m = 1.
 \end{aligned}$$

Here, x_a , x_b , and L_z denote the start and end locations of the blowing and suction region and the spanwise domain size, respectively. We use a frequency of $\beta = 75000$ Hz for the disturbance, with $m_{max} = 5$ and $l_{max} = 10$ and ξ_l and ξ_m being random numbers between 0 and 1.

The free stream Mach number, temperature, and pressure are $Ma_e = 2.25$, $T_e = 169.44$ K, and $p_e = 100000$ Pa, respectively. The Prandtl number and free stream unit Reynolds number are $Pr = 0.72$ and $Re/l_{ref} = \rho_e u_e / \mu_e = 650000$. We use an ideal gas with $\gamma = 1.4$. The temperature dependent dynamic viscosity is computed using the Sutherland law (see Eq. (16)) with $C = 0$, $T_{ref} = T_e$, and $\mu_{ref} = \mu_e$.

We evaluate the mean flow field at the momentum thickness Reynolds number $Re_\theta = \rho_e u_e \theta / \mu_e = 4000$, where θ is the momentum thickness. To compute averages, we collect around 732 time snapshots

over a time period of approximately $1400\delta^*/u_e$, where δ^* denotes the displacement thickness. In the following, we denote mean quantities by $\langle \cdot \rangle$, and the index w describes a quantity at the wall. Figure 10 (a) shows the wall normal profiles of the van-Driest transformed mean velocity

$$\langle u \rangle_{vD}(y) = \int_0^y \sqrt{\frac{\langle \rho \rangle(y')}{\langle \rho \rangle_w}} \frac{d\langle u \rangle(y')}{dy'} dy' \quad (50)$$

normalized by the friction velocity

$$u_\tau = \sqrt{\left. \frac{\langle \mu \rangle}{\langle \rho \rangle} \frac{d\langle u \rangle}{dy} \right|_w}. \quad (51)$$

Figure 10 (b) illustrates the normalized temperature $\langle T \rangle/T_e$, streamwise velocity $\langle u \rangle/u_e$, and streamwise momentum $\langle \rho \rangle \langle u \rangle / \rho_e u_e$. In Fig. 10 (c) we depict the normalized Reynolds stresses $\langle u'_i u'_i \rangle / u_\tau^2 \langle \rho \rangle / \langle \rho \rangle_w$ in stream (u_1), wall normal (u_2), and spanwise direction (u_3). We observe good agreement with the reference DNS [54]. Figure 11 (a) depicts a three-dimensional snapshot of the JAX-Fluids DNS solution. In Fig. 11 (b), we display the skin friction coefficient

$$C_f = 2\tau_w / \rho_e u_e^2, \quad (52)$$

$$\tau_w = \left. \langle \mu \rangle_w \frac{d\langle u \rangle}{dy} \right|_w, \quad (53)$$

along the streamwise Reynolds number $Re_x = \rho_e u_e x / \mu_e$. We observe good agreement with the reference [54] in terms of transition point. A distinct jump of C_f at $Re_x/l_{ref} = 4.55 \times 10^6$ can be seen. This is the intersection point between the first and second zone, where the streamwise grid size is significantly refined. Therefore, this jump is expected. Within the fully developed region

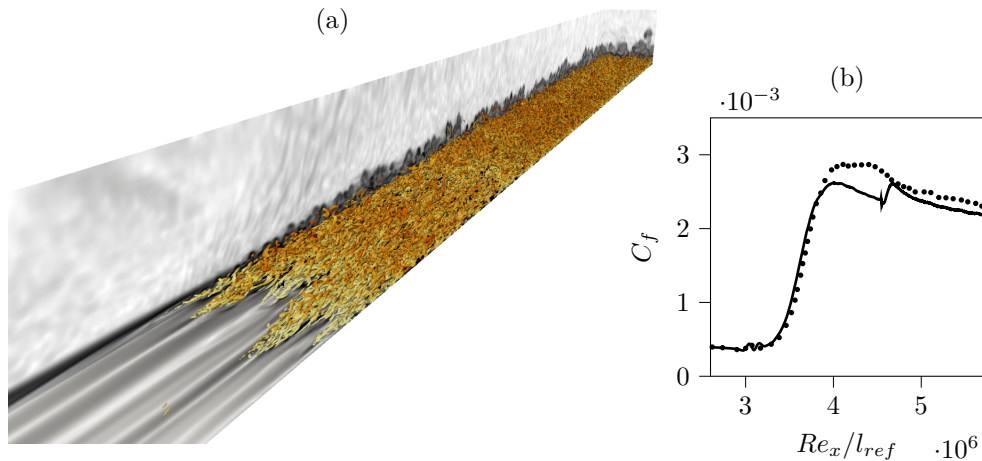


Figure 11: (a) Visualization of the instantaneous flow field showing the transition region. The figure shows contours of the numerical schlieren ($\ln(\|\nabla\rho\|)$) and isosurfaces of the Q criterion colored by the normalized density ρ/ρ_e . (b) Skin friction coefficient C_f as a function of the streamwise Reynolds number Re_x . We illustrate the JAX-Fluids solution with solid lines (—). The reference by Pirozzoli et al. [54] is depicted with markers (\bullet).

Material	x [m]	ρ [kg/m ³]	u [m/s]	p [Pa]	γ [-]	p_∞ [Pa]
Air	$x \leq 0.5$	1.0	0.0	1.0	1.4	0.0
Helium	$x > 0.5$	0.125	0.0	0.1	1.67	0.0

Table 3: Initial conditions and material parameters for the air-helium shock tube.

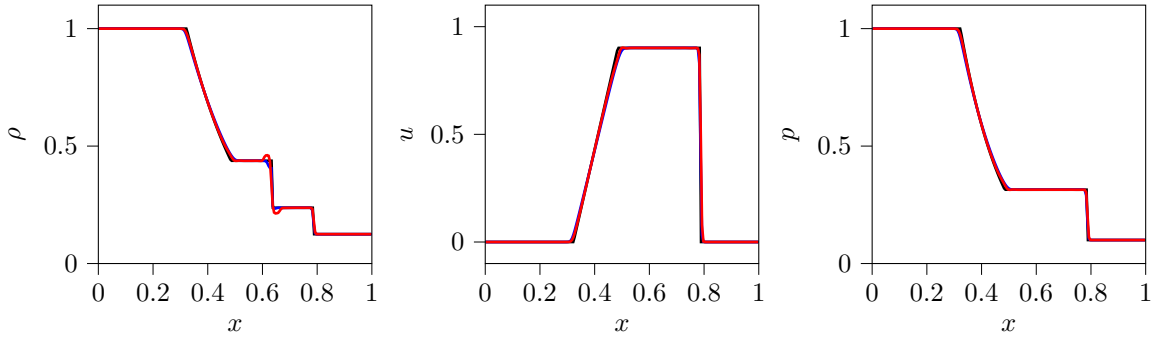


Figure 12: Air-helium shock tube problem visualized at $t = 0.15$. From left to right: density, velocity, and pressure. The exact solution (—) is compared with the level-set result (—) and the diffuse-interface result (—).

$Re_x/l_{ref} \in [4.55 \times 10^6, 5.85 \times 10^6]$, we again have a good match with the reference DNS [54].

5.3. Two-phase simulations

We perform two-phase simulations with the diffuse-interface model (DIM) and the level-set model (LSM). The computation of the cell face fluxes is done with a WENO5-Z reconstruction combined with an HLLC Riemann solver. We use interpolation and flux limiters to ensure physically admissible states. Time integration happens by means of a TVD-RK3 scheme with $CFL = 0.5$. In all DIM simulations, the volume fraction field α_1 is initialized with $1 - 10^{-8}$ in phase 1 and with 10^{-8} in phase 2.

5.3.1. Air-helium shock tube problem

We consider a two-phase gas-gas shock tube problem. The computational domain $x \in [0, 1]$ and is discretized by 200 cells. We use zero gradient boundary conditions at both boundaries. An initial discontinuity at $x = 0.5$ separates air on the left from helium on the right. Initial conditions and material parameters are given in Table 3. Figure 12 shows the solutions at time $t = 0.15$. The reference solution is obtained from an exact Riemann solver [55]. The DIM and LSM results are in very good agreement with the exact solution.

5.3.2. Air-water shock tube problem

We consider a two-phase gas-liquid shock tube problem similarly to [56, 57, 9]. The high density ratio between the two fluids poses more stringent requirements on the numerical scheme. The computational domain $x \in [0.0, 1.5]$ is discretized by 200 cells. We use zero gradient boundary conditions

Material	x [m]	ρ [kg/m ³]	u [m/s]	p [Pa]	γ [-]	p_∞ [Pa]
Water	$x \leq 0.8$	1000.0	0.0	10^9	6.12	3.43×10^8
Air	$x > 0.8$	20.0	0.0	10^5	1.4	0.0

Table 4: Initial conditions and material parameters for the air-water shock tube.

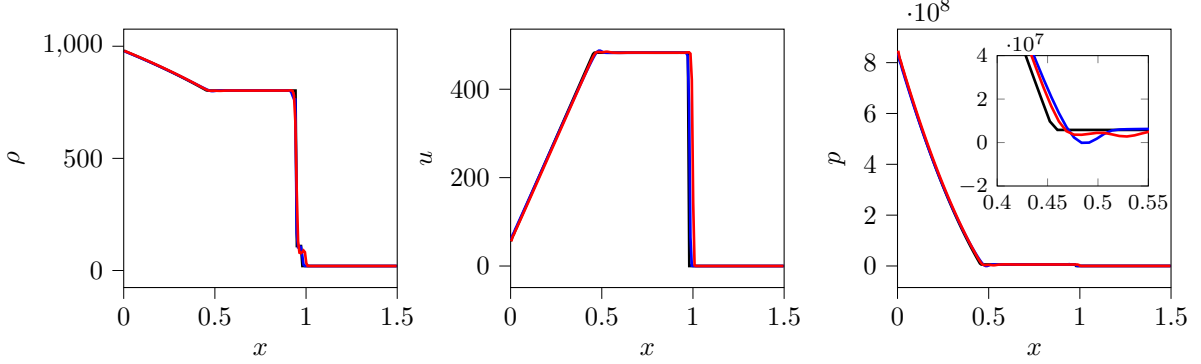


Figure 13: Air-water shock tube problem visualized at $t = 0.15$. From left to right: density, velocity, and pressure. The exact solution (—) is compared with the level-set result (—) and the diffuse-interface result (—).

Case	$l_{channel}$	$h_{channel}$	d_{shock}	d_{bubble}	$D_{0,bubble}$	$N_x \times N_y \times N_z$
Helium SBI 2D	356	89	60	90	50	$4096 \times 1024 \times 1$
Helium SBI 3D	356	89	60	90	45	$3072 \times 768 \times 768$
Water SDI 2D	111	74	20	40	22	$3072 \times 2048 \times 1$
Water SDI 3D	111	74	20	40	22	$1536 \times 1024 \times 1024$

Table 5: Overview on shock bubble interaction simulations. All length scales are in mm.

at both boundaries. An initial discontinuity at $x = 0.8$ separates highly compressed water on the left from air on the right. Initial conditions and material parameters are given in Table 4. Figure 13 shows the solutions at time $t = 0.15$. The reference solution is obtained from an exact Riemann solver [55]. The DIM and LSM results are in very good agreement with the exact solution.

5.3.3. Air-helium shock bubble interaction

The interaction of a shock with a helium bubble immersed in air is a well-documented test case for two-phase flows. Experimental data [58] and numerical reference simulations [59, 17] are available in literature. We perform two- and three-dimensional simulations of the aforementioned shock bubble interaction (SBI) and compare results of the level-set (LSM) and the diffuse-interface (DIM) model with experimental data from Haas et al. [58] and simulation results from Terashima et al. [59]. The setup of the computational domain is detailed in Figure 14 and Table 5. The initial conditions and the material properties are listed in Table 6.

We begin with the two-dimensional test case. The resolution of the two-dimensional simulations

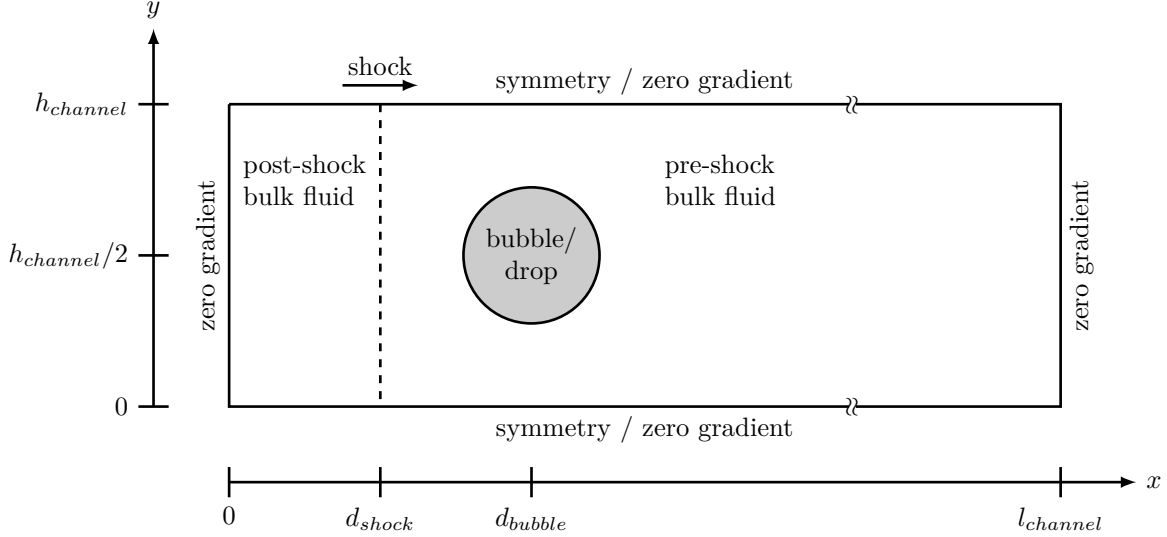


Figure 14: Schematic of the computational domain and the initial configuration for the shock bubble interaction and shock drop interaction simulations.

Case	Incident shock wave	Material	ρ [kg/m ³]	u [m/s]	p [Pa]	γ [-]	p_∞ [Pa]
Helium SBI 2D	$Ma_S = 1.22$	Helium	0.1660	0.0	101325.0	1.67	0.0
	$u_S = 418.746$	Pre-shock air	1.2041	0.0	101325.0	1.4	0.0
	$t_S = 11.940 \times 10^{-6}$	Post-shock air	1.6573	114.5	159056.0		
Helium SBI 3D	$Ma_S = 1.25$	Helium	0.1660	0.0	101325.0	1.67	0.0
	$u_S = 429.043$	Pre-shock air	1.2041	0.0	101325.0	1.4	0.0
	$t_S = 17.481 \times 10^{-6}$	Post-shock air	1.7201	128.7	167819.5		
Water SDI 2D/3D	$Ma_S = 2.40$	Water	1000.0	0.0	101000.0	6.12	3.43×10^8
	$u_S = 834.340$	Pre-shock air	1.17	0.0	101000.0	1.4	0.0
	$t_S = 10.787 \times 10^{-6}$	Post-shock air	3.7579	574.574	661886.67		

Table 6: Initial conditions and material parameters for shock bubble/shock drop interaction simulations.

are 4096×1024 , resulting in approximately $D_0/\Delta x \approx 575$, where D_0 is the initial bubble diameter. Simulations were performed in parallel on 4 Nvidia A6000 GPUs. Figure 15 compares snapshots of the flow field between the numerical simulations and the experiments by Haas et al. [58]. The numerical schlieren from the LSM and DIM simulations are in very good agreement with the experimental schlieren images. Both schemes accurately predict the propagation of the incident shock wave and the reflected waves. The macroscopic bubble shape is in good agreement between the LSM and the DIM. The LSM produces a smoother interface topology while the DIM generates small scale instabilities at the material interface. The smoother interface in the level-set case is attributed to the mixing procedure and first-order reconstruction at the interface. Inspection of the volume fraction fields reveals that

THINC is able to maintain a constant interface thickness over the duration of the simulation as long as interface features are resolved on the given grid. At later times, once finer and finer structures appear, we observe some mixture regions. The LSM conserves a sharp interface. Underresolved structures are eliminated by the reinitialization procedure. Figure 16 compares the temporal evolution of characteristic interface points. Again, both numerical schemes agree very well with the experimental data from [58].

We also compare the three-dimensional SBI with the experimental data of Haas et al. [58]. The resolutions of the three-dimensional simulations are $3072 \times 768 \times 768$. The corresponding resolution of the initial bubble diameter is $D_0/\Delta x \approx 388$. The three-dimensional simulations were done on a TPU v3 256 pod slice. Figure 17 compares snapshots of the flow field. The numerical schlieren for both interface models are in good agreement with the experimental data. Similarly to the 2D results, we observe pronounced interfacial instabilities in the DIM while the LSM maintains a smoother interface.

5.3.4. Air-water shock drop interaction

As a second, more challenging test case for the two-phase schemes, we consider the interaction of a Mach 2.4 shock with a water cylinder (in 2D) and a water drop (in 3D). The high density ratio of the fluids involved poses stringent requirements on the positivity-preserving routine. Experimental data are taken from the work of Sembian et al. [60]. Details on the setup of the computational domain are shown in Figure 14 and Table 5. The initial conditions and material properties are listed in Table 6

We begin with the two-dimensional test case which was run on 4 Nvidia A6000 GPUs. The resolution of the initial bubble diameter is $D_0/\Delta x \approx 608$. Figure 18 shows a comparison between the experimental schlieren images and our simulations. The numerical results for the level-set method (LSM) and the diffuse-interface method (DIM) are in excellent qualitative agreement with the experimental reference data. Especially, both interface models capture very well the propagation of incident, reflected, and transmitted waves. For later stages, we observe fluid being sheared of the rim of the cylinder in the diffuse-interface simulation. Figure 19 shows the numerical schlieren images for the corresponding 3D simulations ($D_0/\Delta x \approx 304$). The three-dimensional simulations were done on a TPU v3 256 pod slice. Again, we observe good agreement between SIM and DIM.

6. Automatic-differentiation gradients

In this section, we showcase the computation of automatic differentiation gradients in the JAX-Fluids framework. In particular, we provide verification for settings in which gradients are calculated across multiple devices.

Figure 20 illustrates two generic scenarios for AD-based gradient calculation in JAX-Fluids. In the first scenario, we are interested in calculating gradients of our quantity of interest with respect to

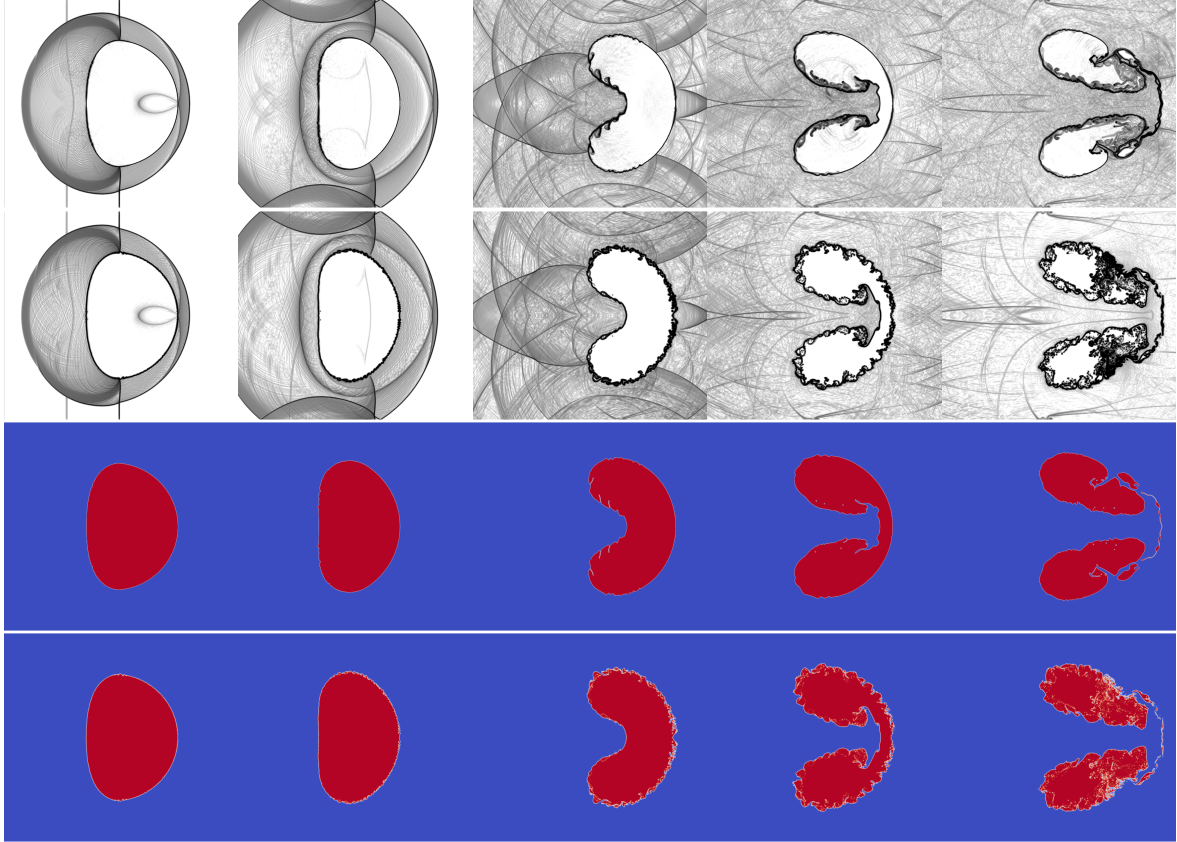


Figure 15: Time series of the two-dimensional air-helium shock bubble interaction. From top to bottom: Numerical schlieren ($\ln(\|\nabla\rho\|)$) from the level-set and diffuse-interface model, volume fraction field from level-set and diffuse-interface model. In the volume fraction fields, red and blue colors represent helium and air, respectively. The snapshots are taken at times $t \in \{72, 102, 245, 427, 674\} \mu\text{s}$ after the incident shock wave has impacted the helium cylinder. (For interpretation of the references to color in this figure legend, the reader is referred to the web version of this article.)
Note: In the arXiv version, experimental images from [58] are not shown due to limited copyrights.

a parameterized initial condition, see Fig. 20a. The function `fun()` consists of three steps: calculation of initial conditions based on the given parameters, forward pass through the JAX-Fluids solver, and calculation of the quantity of interest. If each of these steps is differentiable, we can call the JAX primitive `jax.value_and_grad` to obtain a transformed function which computes the quantity of interest and its derivative with respect to the input parameters `ic_params`. Gradients are backpropagated through `compute_qoi()`, through the entire `feedforward()` routine which comprises multiple integration steps, and, finally, through the `compute_initial_condtion()` routine.

The scenario depicted in Fig. 20b is prototypical of training neural network parameters within the JAX-Fluids framework. Here, `nn_params` should represent weights and biases of a neural network model which is repeatedly being used during forward integration. Similarly to the aforementioned case, gradients of the quantity of interest (e.g., a user-specified loss function) with respect to the

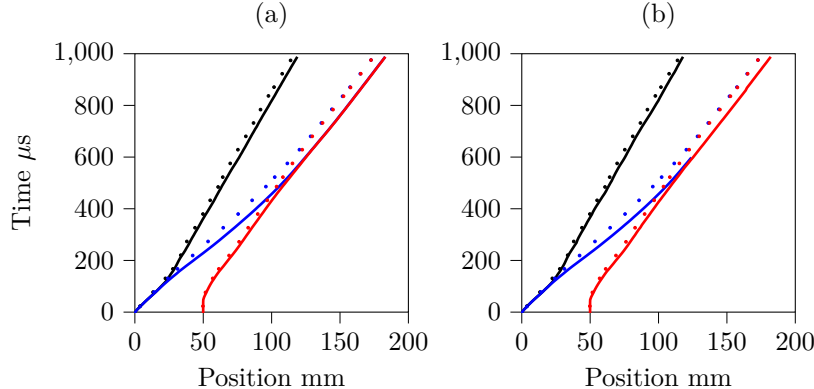


Figure 16: Space-time diagram of three characteristic interface points for the level-set method (left) and the diffuse-interface method (right). Positions of the upstream point (left-most point of the interface, (—)), the jet (left-most point of the interface on the center-line, (—)), and the downstream point (right-most point of the interface, (—)), are depicted as solid lines. Reference values are taken from Terashima et al. [59] and are depicted as markers (\bullet). (For interpretation of the references to color in this figure legend, the reader is referred to the web version of this article.)

parameters `nn_params` are obtained by using the function transformation `jax.value_and_grad`. In [12], we showcase the training of neural networks within JAX-Fluids.

We use *checkpointing* [61] (`jax.checkpoint`) to overcome memory bottlenecks related to the length of the trajectory that is unrolled during the forward pass `feedforward()`. Here, we specify distinct locations (checkpoints) in the computational graph where the state is stored during the forward pass, instead of storing all intermediate results. During the backward pass, we recompute the required intermediate results starting from stored checkpoints. Checkpointing is a trade-off between memory consumption and computation time. Furthermore, we prevent JAX from unrolling the entire trajectory during compilation of `feedforward()` using `jax.lax.scan`, reducing the compilation time significantly.

6.1. Automatic differentiation gradients for a quasi one-dimensional moving shock

To verify automatic-differentiation (AD) gradients for parallel simulations, we investigate the convergence of finite-difference (FD) gradients towards AD gradients. We consider a two-dimensional domain $(x, y) \in [-0.5, 0.5] \times [-0.5, 0.5]$ discretized with 512×512 cells and decomposed using two blocks that are oriented in a 1×2 grid. The flow field is initialized with a discontinuity positioned at $x = 0.0$ describing a quasi one-dimensional moving shock with shock Mach number Ma_S . The pre (index l) and post (index r) conditions depend on Ma_S and are related by the Rankine-Hugoniot conditions [32]. Fixing the post shock state to $p_r = \rho_r = 1.0$ and $u_r = v_r = 0.0$, the initial condition is parameterized solely by Ma_S . For the diffuse-interface (DIM) and level-set (LSM) model, we consider two phases with the interface placed on the shock discontinuity. The specific heat capacity ratio for

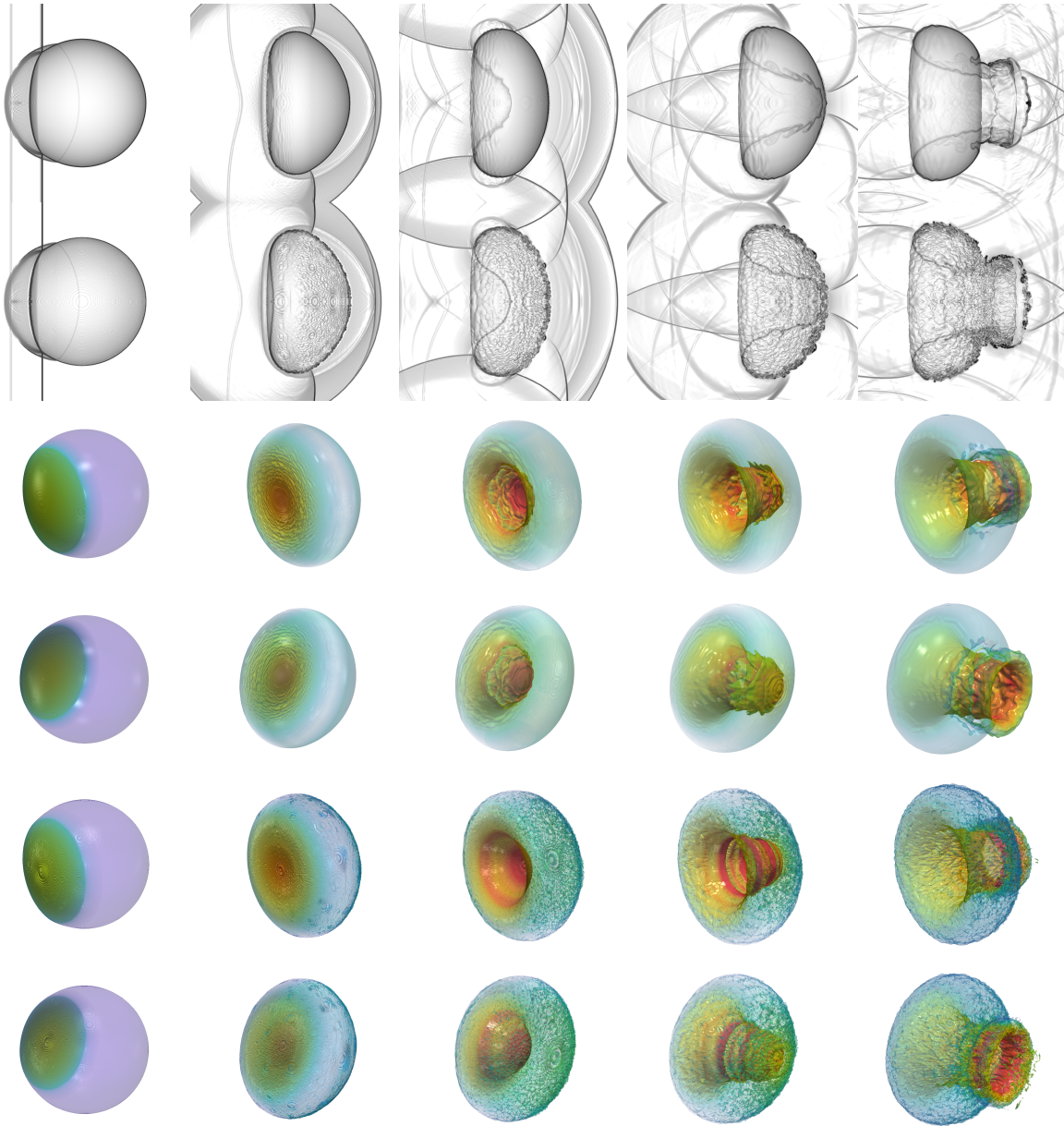


Figure 17: Time series of the three-dimensional air-helium shock bubble interaction. The first two rows show numerical schlieren ($\ln(\|\nabla\rho\|)$) of the level-set (row 1) and diffuse-interface (row 2) model, respectively. The next four rows display the interface contour colored by the absolute velocity. We illustrate the solution of the level-set (row 3 & 4) and the diffuse-interface (row 5 & 6) model, respectively. The snapshots are taken at times $t \in \{20, 82, 145, 223, 350\} \mu\text{s}$ after the incident shock wave has impacted the helium cylinder. (For interpretation of the references to color in this figure legend, the reader is referred to the web version of this article.) **Note: In the arXiv version, experimental images from [58] are not shown due to limited copyrights.**

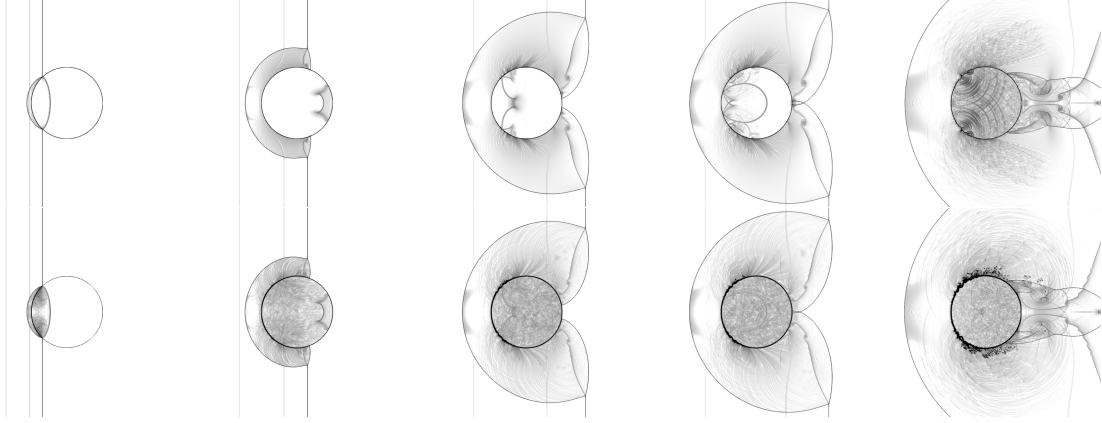


Figure 18: Time series of the two-dimensional air-water shock drop interaction. From top to bottom: Numerical schlieren ($\ln(\|\nabla\rho\|)$) from level-set and the diffuse-interface model. The snapshots are taken at times $t \in \{4, 17, 35, 40, 67\} \mu\text{s}$ after the incident shock wave has impacted the water cylinder. **Note: In the arXiv version, experimental images from [60] are not shown due to limited copyrights.**

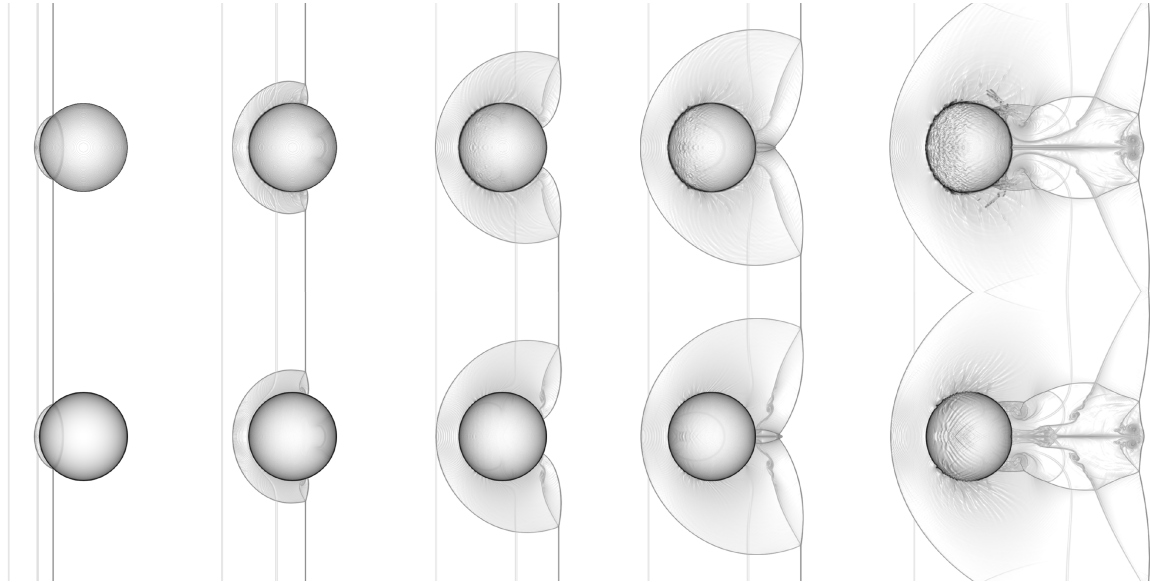


Figure 19: Time series of the three-dimensional air-water shock drop interaction. From top to bottom: Numerical schlieren ($\ln(\|\nabla\rho\|)$) from level-set and the diffuse-interface model. The snapshots are taken at times $t \in \{4, 17, 35, 40, 67\} \mu\text{s}$ after the incident shock wave has impacted the water cylinder.

both phases is $\gamma = 1.4$. As the shock propagates into the quiescent domain, the total energy

$$E(t, Ma_S) = \int_{x,y} \left(\rho e + \frac{1}{2} \rho \mathbf{u} \cdot \mathbf{u} \right) dx dy \quad (54)$$

```

1 import jax
2 from jaxfluids import SimulationManager
3
4 simulation_manager = SimulationManager(
5     "case_setup.json", "numerical_setup.json")
6
7 def fun(ic_params):
8     y0 = compute_initial_condition(ic_params)
9     yn = simulation_manager.feedforward(y0, n_steps)
10    qoi = compute_qoi(yn)
11    return qoi
12
13 fun = jax.value_and_grad(fun)

```

(a)

```

1 import jax
2 from jaxfluids import SimulationManager
3
4 simulation_manager = SimulationManager(
5     "case_setup.json", "numerical_setup.json")
6
7 def fun(nn_params):
8     y0 = compute_initial_condition()
9     yn = simulation_manager.feedforward(y0, n_steps, nn_params)
10    qoi = compute_qoi(yn)
11    return qoi
12
13 fun = jax.value_and_grad(fun)

```

(b)

Figure 20: Code snippets illustrating how to obtain automatic differentiation gradients through a simulation with JAX-Fluids. With `simulation_manager.feedforward()`, the forward simulation through the JAX-Fluids solver is called, and the initial condition is integrated for `n_steps`.

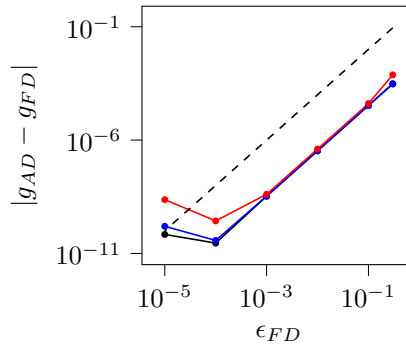


Figure 21: Convergence of finite-difference gradients towards automatic differentiation gradients. The black (\blackrightarrow), blue (\blacklozenge), and red (\blacktriangle) lines indicate the single-phase, diffuse-interface and level-set model, respectively. The black, dashed line ($-$) depicts second-order convergence $\mathcal{O}(\epsilon_{FD}^2)$.

increases. We are interested in the gradient g of the total energy increase $\Delta E^n(Ma_S) = E(t^n, Ma_S) - E(t^0, Ma_S)$ with respect to Ma_S after a fixed amount of time steps n .

$$g = \frac{\partial \Delta E^n(Ma_S)}{\partial Ma_S} \quad (55)$$

We compute this derivative using AD, denoted by g_{AD} , and second-order central FD

$$g_{FD} = \frac{\Delta E^n(Ma_S + \epsilon_{FD}) - \Delta E^n(Ma_S - \epsilon_{FD})}{2\epsilon_{FD}}, \quad (56)$$

where ϵ_{FD} indicates a small number. The computation of g_{AD} requires the differentiation through the entire (parallel) JAX-Fluids algorithm for multiple time steps. The calculation of g_{FD} requires two independent forward simulations.

We choose $Ma_S = 2.0$, $n = 40$, and a fixed time step size of $\Delta t = 10^{-4}$. The numerical setup for all models uses a WENO5-Z spatial reconstruction in combination with an HLLC Riemann solver (Sec. 3.2). The integration is performed using the TVD-RK3 scheme (Sec. 3.4). Figure 21 shows

the convergence of the absolute error $|g_{AD} - g_{FD}|$ with respect to ϵ_{FD} . As expected, we observe second-order convergence for all models. Beyond $\epsilon_{FD} \approx 10^{-4}$, the convergence order starts to reduce due to floating point errors.

6.2. Sensitivities of a helium-air shock bubble interaction

In a second test, we showcase the capability of JAX-Fluids to compute automatic differentiation gradients through extended simulations run in parallel on multi GPU devices. In particular, we are interested in sensitivities of initial conditions on quantities of interest in helium-air shock bubble interaction simulations, see Sec. 5.3.4.

Figure 20a gives a schematic for the computation of sensitivities. We consider an incident shock wave that interacts with a helium-cylinder which is initially at rest. In experimental settings, initial conditions may pose one of the main sources of uncertainty. For example, in the case at hand, there may be uncertainty about the strength of the incident shock or the shape of the initial helium bubble. We want to understand how variations in these parameters may affect quantities of interest. We parameterize the strength of the incident shock by the shock Mach number Ma_S . Additionally, we parameterize the shape of the initial helium bubble by its eccentricity e_b . We require that the mass of the helium bubble is invariant with respect to e_b , i.e., that the area of the bubble at $t = 0$ is constant for varying e_b . Therefore, we define the semi-major axis $a_{bubble} = R_{0,bubble}/(1 - e_b^2)^{0.25}$ and the semi-minor axis $b_{bubble} = R_{0,bubble}(1 - e_b^2)^{0.25}$. Here, $R_{0,bubble}$ is the radius of the circle ($e_b = 0$) with equivalent surface area. a_{bubble} is along the x -direction for positive e_b and along the y -direction for negative e_b . As quantity of interest (QoI), we choose the center of mass drift of the helium bubble Δx_{com}^n in x -direction. Simulations are done with the diffuse-interface model (see Secs. 2.3 and 3.7). The center of mass drift of the helium bubble (fluid 1) is calculated as

$$x_{com}(t) = \frac{\int_{\Omega} \alpha_1 \rho_1 x \, dx dy}{\int_{\Omega} \alpha_1 \rho_1 \, dx dy}, \quad (57)$$

$$\Delta x_{com}^n = x_{com}(t^n) - x_{com}(t = 0). \quad (58)$$

Hence, we are interested in specifying the following sensitivities:

$$\mathbf{g} = [g_1, g_2]^T = \left[\frac{\partial \Delta x_{com}^n}{\partial Ma_S}, \frac{\partial \Delta x_{com}^n}{\partial e_b} \right]^T. \quad (59)$$

Except for shock strength and bubble shape, the computational domain and the initial configuration are the same as in the air-helium SBI case discussed in Sec. 5.3.3. In particular, $R_{0,bubble} = 2.5 \times 10^{-2}$, and the pre-shocked state for air and helium is given in Table 3. The domain is discretized by 512×128 uniform cells. We choose a constant time step $\Delta t = 10^{-7}$ and use TVD-RK3 integration. The center of mass drift is evaluated at $t^n = 10^{-4}$ and $t^n = 2.5 \times 10^{-4}$. This corresponds to a total of $n = 1000$ and $n = 2500$ integration steps, respectively, across which gradients have to be

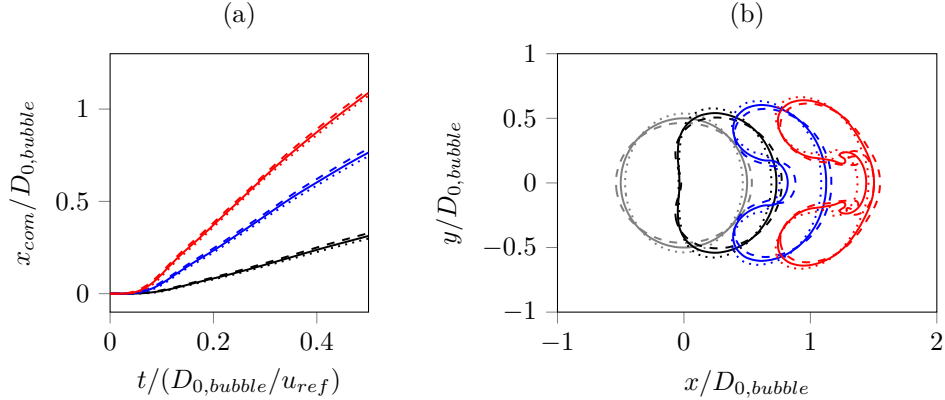


Figure 22: (a) Temporal evolution of the center of mass and (b) interface location at final time $t^n = 2.5 \times 10^{-4}$ for various incident shock Mach numbers Ma_S and initial bubble eccentricities e_b . The shock Mach numbers $Ma_S \in \{1.1, 1.3, 1.5\}$ are depicted as black (—), blue (—), and red (—) lines. The bubble eccentricities $e_b \in \{-0.5, 0.0, 0.5\}$ are depicted as dotted (···), solid (—), and dashed (- -) lines, respectively. The gray lines (—) in (b) visualize the bubble interfaces in the initial configuration ($t = 0$). Spatial coordinates are nondimensionalized with the initial bubble diameter $D_{0,bubble} = 5 \times 10^{-2}$. Time is nondimensionalized with the timescale $D_{0,bubble}/u_{ref}$ where the reference velocity set to $u_{ref} = 100$. (For interpretation of the references to color in this figure legend, the reader is referred to the web version of this article.)

backpropagated. We use checkpoints after every full integration step such that we do not need to keep intermediate values of the Runge-Kutta stages in memory. Each computation is done in parallel on 4 NVIDIA A6000 GPUs. The gradients are evaluated with automatic differentiation and finite differences. Here, we use $\epsilon_{FD} = 10^{-2}$ for the FD gradients. Gradients are computed for $Ma_S \times e_b \in [1.1, 1.5] \times [-0.5, 0.5]$ which is discretized uniformly with 21×21 points. We highlight two important aspects with respect to the computation of the gradients: (i) In order to compute gradients with central finite differences, we need to run two simulations per point of the $Ma_S - e_b$ grid per component of the gradient. For automatic differentiation gradients, however, a single forward run with subsequent backward pass is sufficient for each (Ma_S, e_b) . (ii) The computational effort associated with the AD gradients only increases slightly for each additional sensitivity that we want to compute. This is because the computational graphs for the forward simulation (`feedforward()`) and the computation of the quantity of interest (`compute_qoi()`) remain unchanged, and only the backpropagation through `compute_initial_condition()` has to account for additional sensitivities.

Figure 22 visualizes the nondimensional center of mass drift (a) and the shape of the interface ($\alpha_1 = 0.5$ contour) at $t^n = 2.5 \times 10^{-4}$ (b) for different bubble eccentricities and different incident shock Mach numbers. The strength of the incident shock strongly influences the drift of the helium bubble. The variation in the initial bubble geometry is propagated through the simulation. Figures 23 and 24 show the gradients $g_1 = \frac{\partial \Delta x_{com}^n}{\partial Ma_S}$ and $g_2 = \frac{\partial \Delta x_{com}^n}{\partial e_b}$ obtained by AD and relative errors with respect to the corresponding FD gradients for $t^n = 10^{-4}$ and $t^n = 2.5 \times 10^{-4}$, respectively. At both time instances, AD gradients are in very good agreement with their FD counterparts. We conclude that

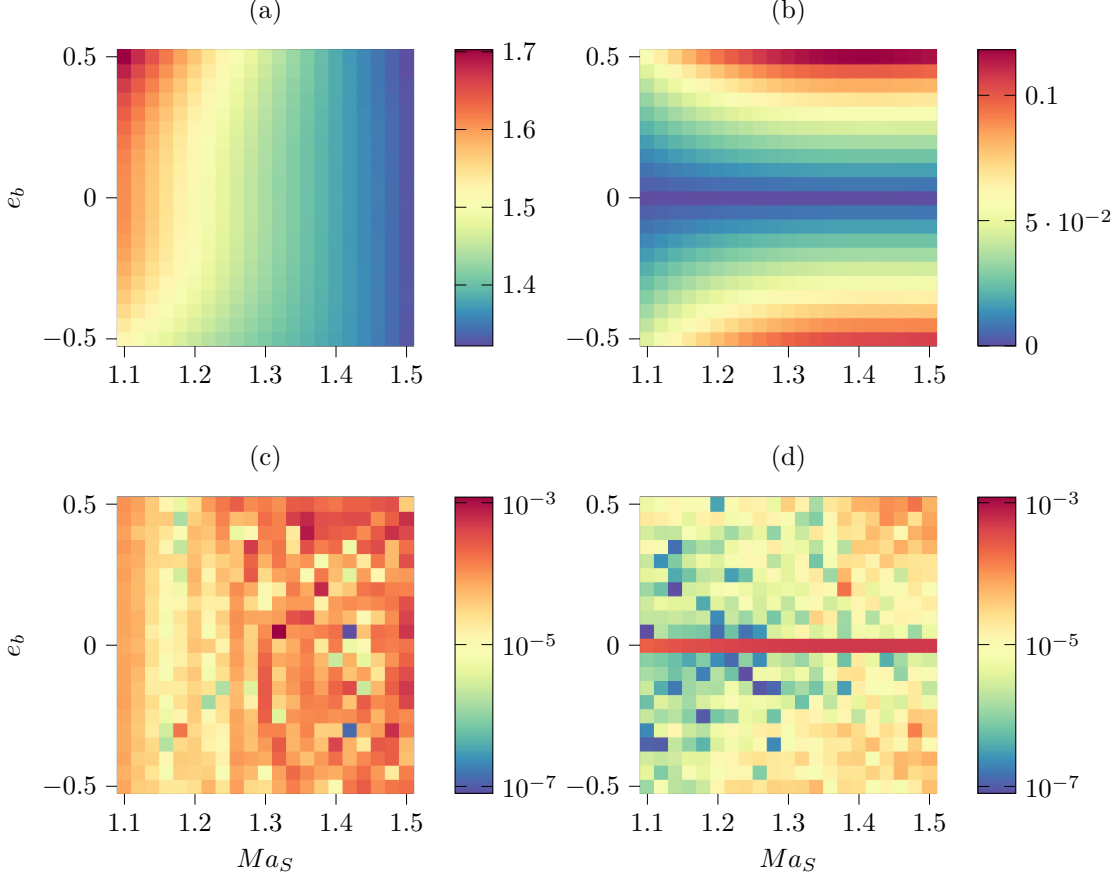


Figure 23: Automatic differentiation gradients of the center of mass drift Δx_{com}^n at $t^n = 10^{-4}$ with respect to incident shock Mach number Ma_S and initial bubble eccentricity e_b . (a): $g_{1,AD} = \left(\frac{\partial \Delta x_{com}^n}{\partial Ma_S} \right)_{AD}$, (b): $g_{2,AD} = \left(\frac{\partial \Delta x_{com}^n}{\partial e_b} \right)_{AD}$, (c): $|g_{1,AD} - g_{1,FD}|/|g_{1,FD}|_\infty$, (d): $|g_{2,AD} - g_{2,FD}|/|g_{2,FD}|_\infty$.

JAX-Fluids allows the parallel evaluation of AD gradients through extended integration trajectories.

7. Parallel performance on GPU and TPU systems

We evaluate the parallel efficiency of JAX-Fluids by performing weak scaling tests of the single-phase (SPM), diffuse-interface (DIM), and level-set model (LSM). The numerical setup consists of the WENO5-Z spatial reconstruction scheme combined with an HLLC approximate Riemann solver (Sec. 3.2). The time integration is performed with the TVD-RK3 scheme (Sec. 3.4).

Within the homogeneous domain decomposition (Sec. 4.2), each XLA device allocates and processes a single block. For the scaling runs, we define a block as a cube of size $1.0 \times 1.0 \times 1.0$ discretized with $N \times N \times N$ cells. We initialize a homogeneous flow field in each block, where the pressure and density are unity and the velocity is zero. For the DIM and the LSM, we consider two phases that are separated by a spherical interface with radius 0.25. The sphere is placed at the center of the block. Periodic boundary conditions are imposed. We perform $M = 200$ integration steps and measure the

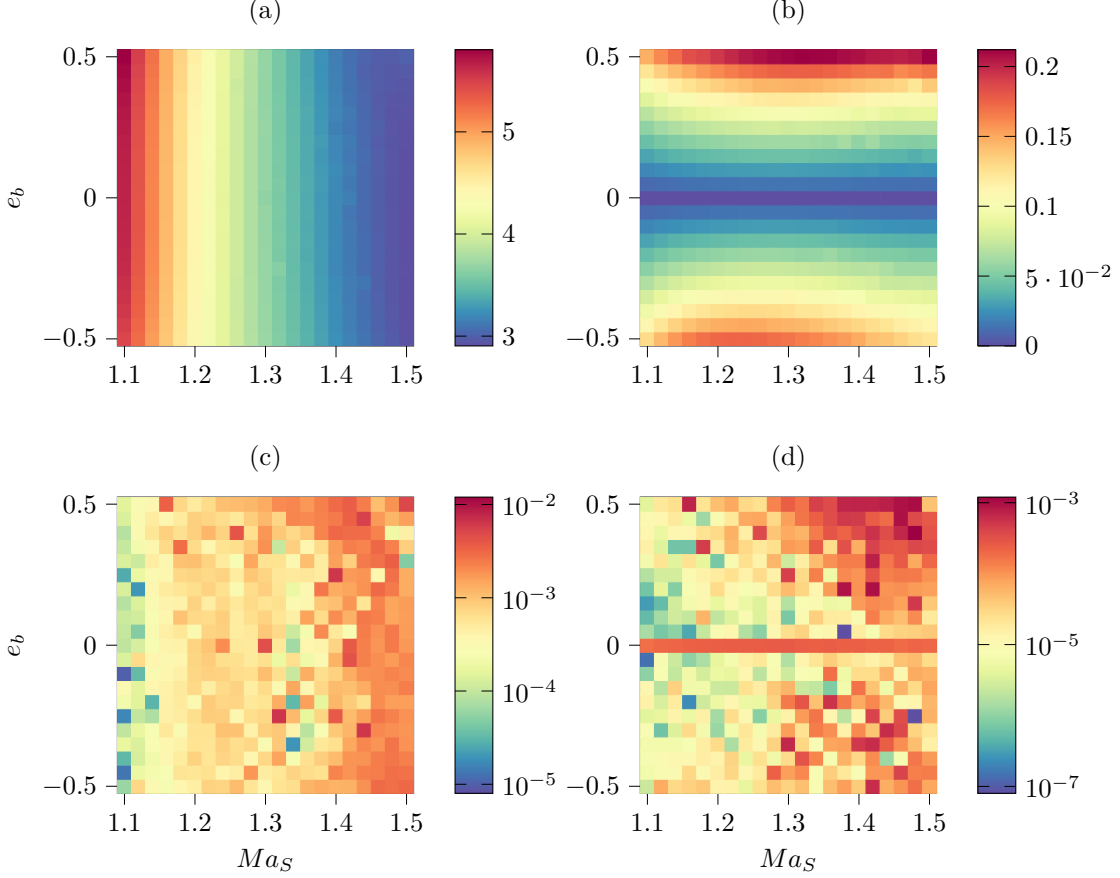


Figure 24: Automatic differentiation gradients of the center of mass drift Δx_{com}^n at $t^n = 2.5 \times 10^{-4}$ with respect to incident shock Mach number Ma_S and initial bubble eccentricity e_b . (a): $g_{1,AD} = \left(\frac{\partial \Delta x_{com}^n}{\partial Ma_S} \right)_{AD}$, (b): $g_{2,AD} = \left(\frac{\partial \Delta x_{com}^n}{\partial e_b} \right)_{AD}$, (c): $|g_{1,AD} - g_{1,FD}|/|g_{1,FD}|_\infty$, (d): $|g_{2,AD} - g_{2,FD}|/|g_{2,FD}|_\infty$.

performance using the mean wall clock time

$$\Delta \bar{T} = \frac{1}{M} \sum_{n=1}^M \Delta T^n. \quad (60)$$

Here, ΔT^n denotes the wall clock time of time step n .

The weak scaling tests are performed on a Google TPU v3 pod and on the JUWELS Booster module at Juelich Supercomputing Centre (JSC). A single node of a TPU v3 consists of 8 TPU v3 cores, each having access to 16GB of RAM. A JUWELS Booster node entails 4 NVIDIA A100 graphics cards with 40GB of RAM each. This means that a single node of the TPU and GPU system has 8 and 4 XLA devices, respectively. It is important to note that the computations on the GPU are performed using double precision, whereas on the TPU, we use single precision. This is because the TPU v3 hardware does not have native support for double precision operations. TPU v3 systems emulate double precision arithmetic in a very costly fashion, reducing the overall performance significantly.

During the weak scaling runs, we successively increase the number of XLA devices (blocks) from 8 up to 1024 on the TPU cluster and from 8 up to 512 on the GPU cluster. We start with 8 XLA devices to ensure that communication occurs in each spatial direction from the get-go, i.e., we start with a domain decomposition of $2 \times 2 \times 2$. Therefore, we begin the scaling with two nodes for the GPU system and with a single node for the TPU system. Table 7 illustrates an overview of the domain decomposition in accordance with the number of nodes. As the table shows, we did not perform a run on a TPU v3 pod slice with 16 cores, as this specific number of cores is not provided by the Google TPU Cloud. Table 8 depicts the resolution of a single block depending on the model and the system. Here, we aim to allocate as much memory as possible on each device, as this ensures that the devices work at their peak efficiency.

We measure the mean wall clock time per time step $\Delta\bar{T}_{S_{XLA}}$ for each number of XLA devices S_{XLA} . The weak scaling represents the normalized mean wall clock time $\omega = \Delta\bar{T}_{S_{XLA}}/\Delta\bar{T}_8$ over the amount of XLA devices (nodes). Figure 25 depicts the weak scaling for both the TPU and GPU system. We observe a very good scaling of $\omega > 0.95$ up to 128 nodes for all models on either system. The largest simulation (SPM, 128 nodes, GPU system) has 16B cells. In terms of scaling efficiency, the TPU v3 pod is slightly better than the NVIDIA A100 GPU system. We depict the reference performance $\Delta\bar{T}_8$ in Table 9. The NVIDIA A100 system clearly outperforms the TPU v3. This is expected, as JAX-Fluids kernels generally operate in the memory bound regime [12], and the NVIDIA A100 has roughly twice as much memory bandwidth compared to the TPU v3.

8. Conclusion

In this work, we have presented the second version of the open-source JAX-Fluids computational fluid dynamics (CFD) solver. Designed as a differentiable solver for compressible single- and two-phase

Nodes	TPU v3		NVIDIA A100 GPU	
	XLA devices	Decomposition	XLA devices	Decomposition
1	8	$2 \times 2 \times 2$	-	-
2	-	-	8	$2 \times 2 \times 2$
4	32	$4 \times 4 \times 2$	16	$4 \times 2 \times 2$
8	64	$4 \times 4 \times 4$	32	$4 \times 4 \times 2$
16	128	$8 \times 4 \times 4$	64	$4 \times 4 \times 4$
32	256	$8 \times 8 \times 4$	128	$8 \times 4 \times 4$
64	512	$8 \times 8 \times 8$	256	$8 \times 8 \times 4$
128	1024	$16 \times 8 \times 8$	512	$8 \times 8 \times 8$

Table 7: Domain decomposition for weak scaling runs. (The Google TPU Cloud did not support a TPU v3 pod slice at the time of the scaling runs.)

XLA Device	SPM	DIM	LSM
NVIDIA A100 GPU	320 ³	288 ³	232 ³
TPU v3	240 ³	184 ³	152 ³

Table 8: Number of cells N^3 per XLA device.

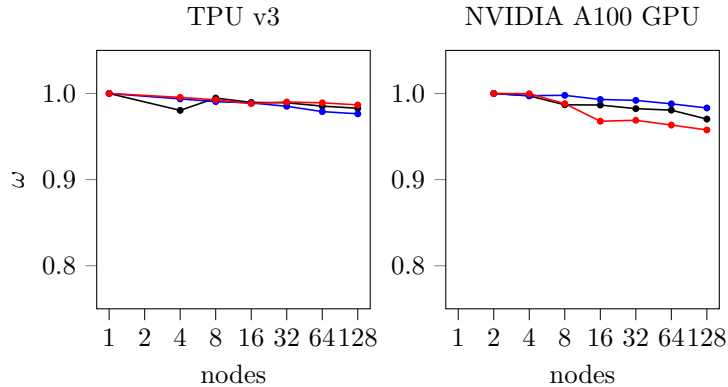


Figure 25: Weak scaling. The black (\blackrightarrow), blue (\blackrightarrow), and red (\blackrightarrow) lines indicate the single-phase, diffuse-interface, and level-set model, respectively.

flows, JAX-Fluids facilitates research at the intersection of conventional CFD and machine learning. Potential research directions for utilizing JAX-Fluids may include data-driven surrogate modeling, data assimilation, uncertainty quantification, and flow control.

With the release of JAX-Fluids 2.0, we propel differentiable CFD towards high performance computing (HPC). The main achievements of our work are summarized as follows.

- JAX Primitives-based Parallelization:** We decompose the computational domain into multiple homogenous blocks and subsequently distribute them across available XLA devices using `jax.pmap`. Data is communicated by collective permutations `jax.lax.ppermute`. The parallelization strategy is validated on GPU and TPU clusters. In particular, we have performed weak scaling runs on up to 512 NVIDIA A100 GPUs and up to 1024 TPU v3 cores. We achieve an excellent weak scaling of > 0.95 for all numerical models.
- Automatic Differentiation (AD) through Parallel Simulations:** The above-mentioned parallelization strategy allows for seamless gradient calculation in distributed computations. Gradients from automatic differentiation are validated against finite-difference gradients, and

XLA Device	SPM	DIM	LSM
NVIDIA A100 GPU	58.01	124.59	332.45
TPU v3	152.73	304.56	1777.99

Table 9: Mean wall clock time per cell $\Delta\bar{T}_8/N^3$ for 8 XLA devices in ns.

we showcase stable AD through trajectories composed of several thousand integration steps.

3. **Diffuse-Interface Two-phase Model:** A five-equation diffuse-interface model for two-phase flows was added. The diffuse-interface model complements the existing level-set based sharp-interface model and allows users to choose between two popular modeling approaches for two-phase flows.

Furthermore, the updated JAX-Fluids package incorporates positivity-preserving limiters, support for stretched Cartesian meshes, refactored I/O routines for increased flexibility and ease of use, performance optimizations, and an updated list of numerical discretization schemes. Newly introduced features to JAX-Fluids have been thoroughly verified by canonical single- and two-phase test cases. In particular, we have shown results for turbulent boundary layer and channel flows, air-helium shock bubble interactions, and air-water shock drop interactions. Good agreement with reference data from literature was achieved.

JAX-Fluids is subject of continuous development, and we highlight two of many areas which we actively pursue.

1. **Multi-Physics Framework:** JAX-Fluids is evolving towards a comprehensive multi-physics framework. This includes, amongst others, the extension to reactive multi-component flows, particle laden flows, phase change phenomena, and fluid-structure interaction.
2. **Adaptive Multiresolution:** The current version of JAX-Fluids employs uniform and stretched Cartesian meshes. Adaptive multiresolution allocates computational resources in regions of interest thereby increasing computational efficiency [62, 63]. The implementation of adaptive multiresolution in differentiable and just-in-time compiled domain-specific languages like JAX is subject of ongoing research.

Acknowledgements

We thank Steffen J. Schmidt, Spencer H. Bryngelson, Qing Wang, and Yi-fan Chen for fruitful discussions throughout this work. TPU computing resources granted by Google’s TRC program are gratefully acknowledged. We also acknowledge GPU computing resources at Juelich Supercomputing Centre (JSC).

Appendix A. Overview Numerical Models

Table A.10 gives an overview on numerical methods implemented in the JAX-Fluids library.

Appendix B. Mesh stretching

JAX-Fluids employs a Cartesian mesh which supports arbitrary one-dimensional mesh stretching. Cell face positions and resulting cell sizes can be strictly monotonous functions of the corresponding

Time Integration	Euler		
	TVD-RK2 [44]		
	TVD-RK3 [44]		
Flux Function/Riemann Solver	Lax-Friedrichs (LxF)	According to [41]	
	Local Lax-Friedrichs (LLxF, Rusanov)	According to [41]	
	HLL/HLLC/HLLC-LM [64, 41, 32, 42, 65]	Signal speed estimates see below	
	AUSM+ [66]		
	Componentwise LLxF	Flux-splitting formulation	
Signal Speed Estimates	Roe [67]	Flux-splitting formulation	
	Arithmetic		
Signal Speed Estimates	Davis [68]		
	Einfeldt [69]		
	Toro [41]		
	Spatial Reconstruction	WENO1 [36]	
		WENO3-JS/Z/N/F3+/NN [36, 70, 71, 72]	
WENO5-JS/Z [36, 33]			
WENO6-CU/CUM [73, 74]			
WENO7-JS [75]			
WENO9-JS [75]			
TENO5/TENO5-A [76, 34]			
TENO6/TENO6-A [76, 34]			
MUSCL [77]		Slope limiters as summarized by [32]	
THINC [37, 38, 39]		For five-equation model only	
2nd-/4th-/6th-order central		For dissipative terms only	
Spatial Derivatives	2nd-/4th-/6th-order central		
	HOUC-3/5/7 [45]		
Level-set reinitialization	First-order [78]		
	HJ-WENO [46]		
Ghost fluid extension	First-order upwind [48]		
LES Modules	ALDM [79]		
Equation of State	Ideal gas		
	Stiffened gas [30]		
	Tait [47]		
Boundary Conditions	Periodic		
	Zero gradient	E.g., used for outflow boundaries	
	Dirichlet		
	No-slip wall		

Table A.10: Overview on numerical methods available in JAX-Fluids.

spatial index. In this work, we use a hyperbolic mesh stretching for the turbulent channel simulation in Sec. 5.2.2. Cell face positions in y -direction are given as

$$y_{i,j-\frac{1}{2},k} = \frac{y_{N_y} - y_0}{2} \cdot \tanh(\beta(2j/N_j - 1)) / \tanh(\beta), j \in [0, N_y], \quad (\text{B.1})$$

For the boundary layer simulations in Secs. 5.2.1 and 5.2.3, we use a hyperbolic stretching given by

$$y_{i,j-\frac{1}{2},k} = (y_{N_y} - y_0) \cdot \tanh(\beta(j/N_j - 1)) / \tanh(\beta) + y_{N_y}, j \in [0, N_y], \quad (\text{B.2})$$

In both cases, β is the stretching parameter.

Appendix C. Spatial discretization

Appendix C.1. Characteristic decomposition

Neglecting viscous terms and source terms, the quasi-linear form of the conservation equation (1) can be reexpressed as

$$\frac{\partial \mathbf{W}}{\partial t} + \mathbf{A}(\mathbf{W}) \frac{\partial \mathbf{W}}{\partial x} + \mathbf{B}(\mathbf{W}) \frac{\partial \mathbf{W}}{\partial y} + \mathbf{C}(\mathbf{W}) \frac{\partial \mathbf{W}}{\partial z} = 0, \quad (\text{C.1})$$

where $\mathbf{A}(\mathbf{W}) = (\partial \mathbf{U} / \partial \mathbf{W})^{-1} \partial \mathbf{F}^c / \partial \mathbf{W}$, $\mathbf{B}(\mathbf{W}) = (\partial \mathbf{U} / \partial \mathbf{W})^{-1} \partial \mathbf{G}^c / \partial \mathbf{W}$, and $\mathbf{C}(\mathbf{W}) = (\partial \mathbf{U} / \partial \mathbf{W})^{-1} \partial \mathbf{H}^c / \partial \mathbf{W}$ are Jacobian matrices associated with the three spatial dimensions. We can find an eigendecomposition for each of these Jacobian matrices. E.g., we decompose $\mathbf{A}(\mathbf{W})$ as

$$\mathbf{A}(\mathbf{W}) = \mathbf{K} \mathbf{\Lambda} \mathbf{K}^{-1}, \quad (\text{C.2})$$

where \mathbf{K} is a matrix whose columns are the right eigenvectors of \mathbf{A} , and $\mathbf{\Lambda}$ is a matrix whose diagonal elements are the corresponding eigenvalues. For the single-phase Navier-Stokes equations, the Jacobian matrix and the matrix of right eigenvectors are given as

$$\mathbf{A} = \begin{bmatrix} u & \rho & 0 & 0 & 0 \\ 0 & u & 0 & 0 & \frac{1}{\rho} \\ 0 & 0 & u & 0 & 0 \\ 0 & 0 & 0 & u & 0 \\ 0 & \rho c^2 & 0 & 0 & u \end{bmatrix}, \quad \mathbf{K} = \begin{bmatrix} \rho & 1 & 0 & 0 & \rho \\ -c & 0 & 0 & 0 & c \\ 0 & 0 & 1 & 0 & 0 \\ 0 & 0 & 0 & 1 & 0 \\ \rho c^2 & 0 & 0 & 0 & \rho c^2 \end{bmatrix}. \quad (\text{C.3})$$

For the five-equation diffuse-interface equations, we find analogous expressions.

$$\mathbf{A} = \begin{bmatrix} u & 0 & \alpha_1 \rho_1 & 0 & 0 & 0 & 0 \\ 0 & u & \alpha_2 \rho_2 & 0 & 0 & 0 & 0 \\ 0 & 0 & u & 0 & 0 & \frac{1}{\rho} & 0 \\ 0 & 0 & 0 & u & 0 & 0 & 0 \\ 0 & 0 & 0 & 0 & u & 0 & 0 \\ 0 & 0 & \rho c^2 & 0 & 0 & u & 0 \\ 0 & 0 & 0 & 0 & 0 & 0 & u \end{bmatrix}, \quad \mathbf{K} = \begin{bmatrix} \alpha_1 \rho_1 & 1 & 0 & 0 & 0 & 0 & \alpha_1 \rho_1 \\ \alpha_2 \rho_2 & 0 & 1 & 0 & 0 & 0 & \alpha_2 \rho_2 \\ -c & 0 & 0 & 0 & 0 & 0 & c \\ 0 & 0 & 0 & 1 & 0 & 0 & 0 \\ 0 & 0 & 0 & 0 & 1 & 0 & 0 \\ \rho c^2 & 0 & 0 & 0 & 0 & 0 & \rho c^2 \\ 0 & 0 & 0 & 0 & 0 & 1 & 0 \end{bmatrix} \quad (\text{C.4})$$

Appendix C.2. HLLC approximate Riemann solver

We specify the wave speeds used in the HLLC Riemann solver, see Sec. 3.2. Following Einfeldt et al. [69], the wave speeds of left and right wave are

$$s^- = \min(0, s^L), \quad (\text{C.5})$$

$$s^+ = \max(0, s^R), \quad (\text{C.6})$$

and

$$s^L = \min(\bar{u} - \bar{c}, u^L - c^L), \quad (\text{C.7})$$

$$s^R = \max(\bar{u} + \bar{c}, u^R + c^R). \quad (\text{C.8})$$

The wave speed for the intermediate wave is chosen following Batten et al. [80]

$$s^* = \frac{p^R - p^L + \rho^L u^L (s^L - u^L) - \rho^R u^R (s^R - u^R)}{\rho^L (s^L - u^L) - \rho^R (s^R - u^R)}. \quad (\text{C.9})$$

Appendix D. Level-set model

Appendix D.1. Interface Riemann Problem

To compute the interface pressure p_Γ and interface velocity \mathbf{u}_Γ , we solve a two-material Riemann problem at the interface. The linearized solution reads [81]

$$\mathbf{u}_\Gamma = \frac{\rho_1 c_1 \mathbf{u}_1 \cdot \mathbf{n}_\Gamma + \rho_2 c_2 \mathbf{u}_2 \cdot \mathbf{n}_\Gamma + p_2 - p_1 - \sigma \kappa}{\rho_1 c_1 + \rho_2 c_2} \mathbf{n}_\Gamma,$$

$$p_\Gamma = \frac{\rho_1 c_1 (p_2) + \rho_2 c_2 p_1 + \rho_1 c_1 \rho_2 c_2 (\mathbf{u}_2 \cdot \mathbf{n}_\Gamma - \mathbf{u}_1 \cdot \mathbf{n}_\Gamma)}{\rho_1 c_1 + \rho_2 c_2},$$

where \mathbf{n}_Γ , ρ , and c denote the interface normal, the density, and the speed of sound, respectively. The subscripts 1 and 2 indicate the two distinct phases.

Appendix D.2. Computation of apertures and volume fraction

We assume a linear approximation of the level-set within each cell. Figure 3 shows a cut cell (i, j, k) with the linear interface segment $\Delta\Gamma_{i,j,k}$ depicted in red. To compute the apertures, we first interpolate the level-set at the vertex points of the cells. The sign of the level-set values at the four vertex points of a cell face determines the general shape of the aperture. A sign change along the edge of a cell face implies an intersection of the interface with the edge. Figure D.26 shows three typical aperture shapes. In total, there are $2^4 = 16$ different sign combinations of the level-set values along the vertices. Hence, there are 16 different aperture shapes. The area of each of these shapes is computed analytically (trapezoid, triangle, etc.). The interface segment $\Delta\Gamma$ is computed from the apertures as

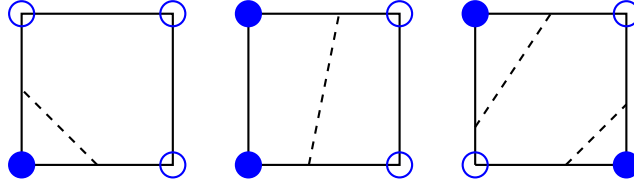


Figure D.26: Three typical aperture shapes. Solid and hollow blue circles indicate positive and negative level-set values, respectively.

follows.

$$\Delta\Gamma_{i,j,k} = \left[\left((A_{i+\frac{1}{2},j,k} - A_{i-\frac{1}{2},j,k})\Delta y\Delta z \right)^2 + \left((A_{i,j+\frac{1}{2},k} - A_{i,j-\frac{1}{2},k})\Delta x\Delta z \right)^2 + \left((A_{i,j,k+\frac{1}{2}} - A_{i,j,k-\frac{1}{2}})\Delta x\Delta y \right)^2 \right]^{\frac{1}{2}}$$

Geometrical reconstruction with seven pyramids yields the volume fraction α .

$$\alpha_{i,j,k} = \frac{1}{3} \frac{1}{\Delta x\Delta y\Delta z} \left[A_{i+\frac{1}{2},j,k}\Delta y\Delta z\frac{1}{2}\Delta x + A_{i-\frac{1}{2},j,k}\Delta y\Delta z\frac{1}{2}\Delta x + A_{i,j+\frac{1}{2},k}\Delta x\Delta z\frac{1}{2}\Delta y + A_{i,j-\frac{1}{2},k}\Delta x\Delta z\frac{1}{2}\Delta y + A_{i,j,k+\frac{1}{2}}\Delta x\Delta y\frac{1}{2}\Delta z + A_{i,j,k-\frac{1}{2}}\Delta x\Delta y\frac{1}{2}\Delta z + A_{i,j,k+\frac{1}{2}}\Delta x\Delta y\frac{1}{2}\Delta z + \Delta\Gamma_{i,j,k}\phi_{i,j,k} \right]$$

The described approach yields the volume fraction and apertures with respect to the positive phase.

Appendix D.3. Conservative mixing procedure

The presented level-set method (see Sec. 3.6) is not consistent when the interface crosses a cell face within a single time step, i.e., when new cells are created or cells have vanished. Furthermore, small cut cells may lead to an unstable integration using the time step restriction that is based on a full cell. We apply a mixing procedure [48, 49] that deals with both of these problems. There are three types of cells that require mixing

1. Cells for which $\alpha = 0$ after integration but $\alpha \neq 0$ before (vanished cells).
2. Cells for which $\alpha > 0$ after integration but $\alpha = 0$ before (newly created cells).
3. Cells for which $\alpha < \alpha_{\text{mix}}$ after integration (small cells).

Here, α_{mix} is a specified threshold. We identify neighboring, target (subscript trg) cells from the interface normal. One in each spatial direction x , y , and z , one in each plane xy , xz , and yz , and one in xyz . Seven mixing weights are computed as

$$\begin{aligned}
\beta_x &= |\mathbf{n}_\Gamma \cdot \mathbf{i}|^2 \alpha_{\text{trg}}, \\
\beta_y &= |\mathbf{n}_\Gamma \cdot \mathbf{j}|^2 \alpha_{\text{trg}}, \\
\beta_z &= |\mathbf{n}_\Gamma \cdot \mathbf{k}|^2 \alpha_{\text{trg}}, \\
\beta_{xy} &= |(\mathbf{n}_\Gamma \cdot \mathbf{i})(\mathbf{n}_\Gamma \cdot \mathbf{j})| \alpha_{\text{trg}}, \\
\beta_{xz} &= |(\mathbf{n}_\Gamma \cdot \mathbf{i})(\mathbf{n}_\Gamma \cdot \mathbf{k})| \alpha_{\text{trg}}, \\
\beta_{yz} &= |(\mathbf{n}_\Gamma \cdot \mathbf{j})(\mathbf{n}_\Gamma \cdot \mathbf{k})| \alpha_{\text{trg}}, \\
\beta_{xyz} &= |(\mathbf{n}_\Gamma \cdot \mathbf{i})(\mathbf{n}_\Gamma \cdot \mathbf{j})(\mathbf{n}_\Gamma \cdot \mathbf{k})|^{2/3} \alpha_{\text{trg}},
\end{aligned} \tag{D.1}$$

where \mathbf{i} , \mathbf{j} , and \mathbf{k} are the unit vectors in x , y , and z direction. We normalize the mixing weights so that $\sum_{\text{trg}} \beta_{\text{trg}} = 1$, where $\text{trg} \in \{x, y, z, xy, xz, yz, xyz\}$. Subsequently, the mixing flux \mathbf{M}_{trg} is computed as

$$\mathbf{M}_{\text{trg}} = \frac{\beta_{\text{trg}}}{\alpha \beta_{\text{trg}} + \alpha_{\text{trg}}} [(\alpha_{\text{trg}} \bar{\mathbf{U}}_{\text{trg}}) \alpha - (\alpha \bar{\mathbf{U}}) \alpha_{\text{trg}}]. \tag{D.2}$$

The conservative variables are then updated according to

$$\alpha \bar{\mathbf{U}} = (\alpha \bar{\mathbf{U}})^* + \sum_{\text{trg}} \mathbf{M}_{\text{trg}}, \tag{D.3}$$

$$\alpha_{\text{trg}} \bar{\mathbf{U}}_{\text{trg}} = (\alpha_{\text{trg}} \bar{\mathbf{U}}_{\text{trg}})^* - \sum_{\text{trg}} \mathbf{M}_{\text{trg}}. \tag{D.4}$$

Here, $\alpha \bar{\mathbf{U}}$ and $\alpha_{\text{trg}} \bar{\mathbf{U}}_{\text{trg}}$ denote the conservative variables of the cells that require mixing and the conservative variables of the corresponding target cells, respectively. Star-quantities denote conservative variables before mixing. The mixing procedure is performed on the integrated conservative variables.

Data Availability Statement

JAX-Fluids is available under the GNU GPLv3 license at <https://github.com/tumaer/JAXFLUIDS>.

References

- [1] S. L. Brunton, B. R. Noack, P. Koumoutsakos, Machine learning for fluid mechanics, *Annual Review of Fluid Mechanics* 52 (2020) 477–508. doi:10.1146/annurev-fluid-010719-060214.
- [2] R. Vinuesa, S. L. Brunton, Enhancing computational fluid dynamics with machine learning, *Nature Computational Science* 2 (2022) 358–366. doi:10.1038/s43588-022-00264-7.
URL <https://www.nature.com/articles/s43588-022-00264-7>
- [3] A. G. Baydin, B. A. Pearlmutter, J. M. Siskind, Automatic differentiation in machine learning: a survey, *Journal of Machine Learning Research* 18 (2017) 5595–5637.
- [4] M. Abadi, P. Barham, J. Chen, Z. Chen, A. Davis, J. Dean, M. Devin, S. Ghemawat, G. Irving, M. Isard, M. Kudlur, J. Levenberg, R. Monga, S. Moore, D. G. Murray, B. Steiner, P. Tucker, V. Vasudevan, P. Warden, M. Wicke, Y. Yu, X. Zheng, G. Brain, Tensorflow: A system for large-scale machine learning tensorflow: A system for large-scale machine learning, *Proceedings of the 12th USENIX Symposium on Operating Systems Design and Implementation* (2016).
URL <https://tensorflow.org>.
- [5] A. Paszke, S. Gross, F. Massa, A. Lerer, J. Bradbury, G. Chanan, T. Killeen, Z. Lin, N. Gimelshein, L. Antiga, A. Desmaison, A. Köpf, E. Yang, Z. DeVito, M. Raison, A. Tejani, S. Chilamkurthy, B. Steiner, L. Fang, J. Bai, S. Chintala, Pytorch: An imperative style, high-performance deep learning library, Vol. 32, 2019.
- [6] J. Bradbury, R. Frostig, P. Hawkins, M. J. Johnson, C. Leary, D. Maclaurin, G. Necula, A. Paszke, J. Vanderplas, S. Wanderman-Milne, Q. Zhang, {JAX}: composable transformations of {Python}+{NumPy} programs (2018).
- [7] S. S. Schoenholz, E. D. Cubuk, Jax, m.d. a framework for differentiable physics, Vol. 2020-December, *Neural information processing systems foundation*, 2020.
- [8] D. Kochkov, J. A. Smith, A. Alieva, Q. Wang, M. P. Brenner, S. Hoyer, Machine learning accelerated computational fluid dynamics (2021) 1–13 [arXiv:2102.01010](https://arxiv.org/abs/2102.01010).
URL <http://arxiv.org/abs/2102.01010>
- [9] Q. Wang, M. Ihme, Y. F. Chen, J. Anderson, A TensorFlow simulation framework for scientific computing of fluid flows on tensor processing units, *Computer Physics Communications* 274 (aug 2022). [arXiv:2108.11076](https://arxiv.org/abs/2108.11076), doi:10.1016/j.cpc.2022.108292.
URL <http://arxiv.org/abs/2108.11076><http://dx.doi.org/10.1016/j.cpc.2022.108292>
- [10] M. Ataei, H. Salehipour, Xlb: A differentiable massively parallel lattice boltzmann library in python (11 2023).
URL <http://arxiv.org/abs/2311.16080>

- [11] T. Xue, S. Liao, Z. Gan, C. Park, X. Xie, W. K. Liu, J. Cao, Jax-fem: A differentiable gpu-accelerated 3d finite element solver for automatic inverse design and mechanistic data science (12 2022). doi:10.1016/j.cpc.2023.108802.
URL <http://arxiv.org/abs/2212.00964><http://dx.doi.org/10.1016/j.cpc.2023.108802>
- [12] D. A. Bezgin, A. B. Buhendwa, N. A. Adams, JAX-FLUIDS: A fully-differentiable high-order computational fluid dynamics solver for compressible two-phase flows, *Computer Physics Communications* 282 (2022) 108527. arXiv:2203.13760, doi:10.1016/j.cpc.2022.108527.
URL <http://arxiv.org/abs/2203.13760>
- [13] R. Frostig, M. J. Johnson, C. Leary, Compiling machine learning programs via high-level tracing, 2018.
- [14] C. R. Harris, K. J. Millman, S. J. van der Walt, R. Gommers, P. Virtanen, D. Cournapeau, E. Wieser, J. Taylor, S. Berg, N. J. Smith, R. Kern, M. Picus, S. Hoyer, M. H. van Kerkwijk, M. Brett, A. Haldane, J. F. del R  o, M. Wiebe, P. Peterson, P. G  rard-Marchant, K. Sheppard, T. Reddy, W. Weckesser, H. Abbasi, C. Gohlke, T. E. Oliphant, *Array programming with numpy* (2020). doi:10.1038/s41586-020-2649-2.
URL <https://doi.org/10.1038/s41586-020-2649-2>
- [15] S. Osher, J. A. Sethian, Fronts propagating with curvature-dependent speed: Algorithms based on hamilton-jacobi formulations, *Journal of Computational Physics* 79 (1988) 12–49. doi:10.1016/0021-9991(88)90002-2.
- [16] M. Sussman, A level set approach for computing solutions to incompressible two-phase flow, *Journal of Computational Physics* 114 (1) (1994) 146–159. doi:10.1006/jcph.1994.1155.
- [17] N. Hoppe, J. M. Winter, S. Adami, N. A. Adams, ALPACA - a level-set based sharp-interface multiresolution solver for conservation laws, *Computer Physics Communications* 272 (2022) 108246. doi:10.1016/j.cpc.2021.108246.
URL <https://linkinghub.elsevier.com/retrieve/pii/S0010465521003581>
- [18] G. Allaire, S. Clerc, S. Kokh, A five-equation model for the simulation of interfaces between compressible fluids, *Journal of Computational Physics* 181 (2002) 577–616. doi:10.1006/jcph.2002.7143.
URL <https://linkinghub.elsevier.com/retrieve/pii/S0021999102971433>
- [19] G. Perigaud, R. Saurel, A compressible flow model with capillary effects, *Journal of Computational Physics* 209 (2005) 139–178. doi:10.1016/j.jcp.2005.03.018.
URL <https://linkinghub.elsevier.com/retrieve/pii/S0021999105001853>

- [20] V. Coralic, T. Colonius, Finite-volume WENO scheme for viscous compressible multicomponent flows, *Journal of Computational Physics* 274 (2014) 95–121. doi:10.1016/j.jcp.2014.06.003. URL <https://linkinghub.elsevier.com/retrieve/pii/S0021999114004082>
- [21] M. L. Wong, J. B. Angel, M. F. Barad, C. C. Kiris, A positivity-preserving high-order weighted compact nonlinear scheme for compressible gas-liquid flows, *Journal of Computational Physics* 444 (2021) 110569. doi:10.1016/j.jcp.2021.110569. URL <https://linkinghub.elsevier.com/retrieve/pii/S0021999121004642>
- [22] A. Beck, D. Flad, C. D. Munz, Deep neural networks for data-driven LES closure models, *Journal of Computational Physics* 398 (2019). doi:10.1016/j.jcp.2019.108910.
- [23] J. Sirignano, J. F. MacArt, J. B. Freund, Dpm: A deep learning pde augmentation method with application to large-eddy simulation, *Journal of Computational Physics* 423 (12 2020). doi:10.1016/j.jcp.2020.109811.
- [24] D. A. Bezgin, S. J. Schmidt, N. A. Adams, A data-driven physics-informed finite-volume scheme for nonclassical undercompressive shocks, *Journal of Computational Physics* 437 (2021) 110324. doi:10.1016/j.jcp.2021.110324. URL <https://linkinghub.elsevier.com/retrieve/pii/S0021999121002199>
- [25] M. Raissi, P. Perdikaris, G. E. Karniadakis, Physics-informed neural networks: A deep learning framework for solving forward and inverse problems involving nonlinear partial differential equations, *Journal of Computational Physics* 378 (2019) 686–707. doi:10.1016/j.jcp.2018.10.045.
- [26] A. B. Buhendwa, S. Adami, N. A. Adams, Inferring incompressible two-phase flow fields from the interface motion using physics-informed neural networks, *Machine Learning with Applications* 4 (2021) 100029. doi:10.1016/j.mlwa.2021.100029. URL <https://doi.org/10.1016/j.mlwa.2021.100029>
- [27] A. D. Jagtap, Z. Mao, N. Adams, G. E. Karniadakis, Physics-informed neural networks for inverse problems in supersonic flows, *Journal of Computational Physics* 466 (2022) 111402. doi:10.1016/j.jcp.2022.111402. URL <https://linkinghub.elsevier.com/retrieve/pii/S0021999122004648>
- [28] P. Karnakov, S. Litvinov, P. Koumoutsakos, Optimizing a DIscrete Loss (ODIL) to solve forward and inverse problems for partial differential equations using machine learning tools (2022) 1–7arXiv:2205.04611. URL <http://arxiv.org/abs/2205.04611>
- [29] E. Johnsen, T. Colonius, Implementation of weno schemes in compressible multicomponent flow problems, *Journal of Computational Physics* 219 (2006) 715–732. doi:10.1016/j.jcp.2006.04.

018.

URL <https://linkinghub.elsevier.com/retrieve/pii/S0021999106002014>

- [30] R. Menikoff, B. J. Plohr, The riemann problem for fluid flow of real materials, *Reviews of Modern Physics* 61 (1989) 75–130. doi:10.1103/RevModPhys.61.75.
- [31] W. Sutherland, Lii. the viscosity of gases and molecular force, *The London, Edinburgh, and Dublin Philosophical Magazine and Journal of Science* 36 (1893) 507–531. doi:10.1080/14786449308620508.
- [32] E. F. Toro, *Riemann solvers and numerical methods for fluid dynamics a practical introduction*, 3rd Edition, Springer Verlag, 2009.
- [33] R. Borges, M. Carmona, B. Costa, W. S. Don, An improved weighted essentially non-oscillatory scheme for hyperbolic conservation laws, *Journal of Computational Physics* 227 (2008) 3191–3211. doi:10.1016/j.jcp.2007.11.038.
- [34] L. Fu, X. Y. Hu, N. A. Adams, Improved five- and six-point targeted essentially nonoscillatory schemes with adaptive dissipation, *AIAA Journal* 57 (2019) 1143–1158. doi:10.2514/1.J057370. URL <https://arc.aiaa.org/doi/10.2514/1.J057370>
- [35] C.-W. Shu, Essentially non-oscillatory and weighted essentially non-oscillatory schemes for hyperbolic conservation laws, 1998, pp. 325–432. doi:10.1007/BFb0096355. URL <http://link.springer.com/10.1007/BFb0096355>
- [36] G. S. Jiang, C. W. Shu, Efficient implementation of weighted eno schemes, *Journal of Computational Physics* 126 (1996) 202–228. doi:10.1006/jcph.1996.0130.
- [37] F. Xiao, Y. Honma, T. Kono, A simple algebraic interface capturing scheme using hyperbolic tangent function, *International Journal for Numerical Methods in Fluids* 48 (2005) 1023–1040. doi:10.1002/flid.975. URL <https://onlinelibrary.wiley.com/doi/10.1002/flid.975>
- [38] F. Xiao, S. Ii, C. Chen, Revisit to the thinc scheme: A simple algebraic vof algorithm, *Journal of Computational Physics* 230 (2011) 7086–7092. doi:10.1016/j.jcp.2011.06.012. URL <https://linkinghub.elsevier.com/retrieve/pii/S0021999111003615>
- [39] K.-M. Shyue, F. Xiao, An eulerian interface sharpening algorithm for compressible two-phase flow: The algebraic thinc approach, *Journal of Computational Physics* 268 (2014) 326–354. doi:10.1016/j.jcp.2014.03.010. URL <https://linkinghub.elsevier.com/retrieve/pii/S0021999114001831>

- [40] D. P. Garrick, W. A. Hagen, J. D. Regele, An interface capturing scheme for modeling atomization in compressible flows, *Journal of Computational Physics* 344 (2017) 260–280. doi:10.1016/j.jcp.2017.04.079.
URL <https://linkinghub.elsevier.com/retrieve/pii/S0021999117303674>
- [41] E. F. Toro, M. Spruce, W. Speares, Restoration of the contact surface in the hll-riemann solver, *Shock waves* 4 (1994) 25–34.
URL <http://link.springer.com/article/10.1007/BF01414629><https://link.springer.com/content/pdf/10.1007%2FBF01414629.pdf>
- [42] E. F. Toro, The hllc riemann solver, *Shock Waves* 29 (2019) 1065–1082. doi:10.1007/s00193-019-00912-4.
URL <https://doi.org/10.1007/s00193-019-00912-4>
- [43] X. Y. Hu, N. A. Adams, C.-W. Shu, Positivity-preserving method for high-order conservative schemes solving compressible euler equations, *Journal of Computational Physics* 242 (2013) 169–180. doi:10.1016/j.jcp.2013.01.024.
URL <https://linkinghub.elsevier.com/retrieve/pii/S0021999113000557>
- [44] S. Gottlieb, C.-W. Shu, Total variation diminishing runge-kutta schemes, *Mathematics of computation of the American Mathematical Society* 67 (1998) 73–85.
URL <http://www.ams.org/mcom/1998-67-221/S0025-5718-98-00913-2/>
- [45] R. R. Nourgaliev, T. G. Theofanous, High-fidelity interface tracking in compressible flows: Unlimited anchored adaptive level set, *Journal of Computational Physics* 224 (2007) 836–866. doi:10.1016/j.jcp.2006.10.031.
URL <http://linkinghub.elsevier.com/retrieve/pii/S0021999106005511>
- [46] G. S. Jiang, D. Peng, Weighted eno schemes for hamilton-jacobi equations, *SIAM Journal on Scientific Computing* 21 (2000) 2126–2143. doi:10.1137/S106482759732455X.
URL <http://www.siam.org/journals/ojsa.php>
- [47] R. P. Fedkiw, T. Aslam, B. Merriman, S. Osher, A non-oscillatory eulerian approach to interfaces in multimaterial flows (the ghost fluid method), *Journal of Computational Physics* 152 (1999) 457–492. doi:10.1006/jcph.1999.6236.
- [48] X. Y. Hu, B. C. Khoo, N. A. Adams, F. L. Huang, A conservative interface method for compressible flows, *J. Comput. Phys.* 219 (2006) 553–578. doi:10.1016/j.jcp.2006.04.001.
URL <http://linkinghub.elsevier.com/retrieve/pii/S0021999106001926>
- [49] E. Lauer, X. Y. Hu, S. Hickel, N. A. Adams, Numerical modelling and investigation of symmetric and asymmetric cavitation bubble dynamics, *Computers & Fluids* 69 (2012) 1–19. doi:10.1016/

- j.compfluid.2012.07.020.
 URL <http://linkinghub.elsevier.com/retrieve/pii/S0045793012002885>
- [50] D. Häfner, F. Vicentini, mpi4jax: Zero-copy mpi communication of jax arrays, *Journal of Open Source Software* 6 (2021) 3419. doi:10.21105/joss.03419.
 URL <https://joss.theoj.org/papers/10.21105/joss.03419>
- [51] F. M. White, *Viscous Fluid Flow*, 2nd Edition, McGraw Hill Higher Education, Maidenhead, England, 1991.
- [52] G. N. Coleman, J. Kim, R. D. Moser, A numerical study of turbulent supersonic isothermal-wall channel flow, *Journal of Fluid Mechanics* 305 (1995) 159–183. doi:10.1017/S0022112095004587.
 URL https://www.cambridge.org/core/product/identifier/S0022112095004587/type/journal_article
- [53] R. Lechner, J. Sesterhenn, R. Friedrich, Turbulent supersonic channel flow, *Journal of Turbulence* 2 (2001) N1. doi:10.1088/1468-5248/2/1/001.
 URL <http://www.tandfonline.com/doi/abs/10.1088/1468-5248/2/1/001>
- [54] S. Pirozzoli, F. Grasso, T. B. Gatski, Direct numerical simulation and analysis of a spatially evolving supersonic turbulent boundary layer at $M = 2.25$, *Physics of Fluids* 16 (3) (2004) 530–545. doi:10.1063/1.1637604.
- [55] D. ZEIDAN, A. SLAOUTI, E. ROMENSKI, E. F. TORO, Numerical solution for hyperbolic conservative two-phase flow equations, *International Journal of Computational Methods* 04 (2007) 299–333. doi:10.1142/S0219876207000984.
 URL <https://www.worldscientific.com/doi/abs/10.1142/S0219876207000984>
- [56] R. Abgrall, S. Karni, Computations of compressible multifluids, *Journal of Computational Physics* 169 (2001) 594–623. doi:10.1006/jcph.2000.6685.
 URL <https://linkinghub.elsevier.com/retrieve/pii/S0021999100966853>
- [57] H. Chen, S. M. Liang, Flow visualization of shock/water column interactions, *Shock Waves* 17 (2008) 309–321. doi:10.1007/s00193-007-0115-9.
- [58] J.-F. Haas, B. Sturtevant, Interaction of weak shock waves with cylindrical and spherical gas inhomogeneities, *Journal of Fluid Mechanics* 181 (1987) 41. doi:10.1017/S0022112087002003.
 URL http://www.journals.cambridge.org/abstract_S0022112087002003
- [59] H. Terashima, G. Tryggvason, A front-tracking/ghost-fluid method for fluid interfaces in compressible flows, *Journal of Computational Physics* 228 (2009) 4012–4037. doi:10.1016/j.jcp.2009.02.023.
 URL <https://linkinghub.elsevier.com/retrieve/pii/S0021999109000898>

- [60] S. Sembian, M. Liverts, N. Tillmark, N. Apazidis, Plane shock wave interaction with a cylindrical water column, *Physics of Fluids* 28 (2016). doi:10.1063/1.4948274.
URL <http://dx.doi.org/10.1063/1.4948274>
- [61] C. C. Margossian, A review of automatic differentiation and its efficient implementation, *WIREs Data Mining and Knowledge Discovery* 9 (7 2019). doi:10.1002/widm.1305.
URL <https://wires.onlinelibrary.wiley.com/doi/10.1002/widm.1305>
- [62] A. Harten, Adaptive multiresolution schemes for shock computations, *Journal of Computational Physics* 115 (1994) 319–338. doi:10.1006/jcph.1994.1199.
URL <https://linkinghub.elsevier.com/retrieve/pii/S0021999184711995>
- [63] A. Harten, Multiresolution algorithms for the numerical solution of hyperbolic conservation laws, *Communications on Pure and Applied Mathematics* 48 (1995) 1305–1342. doi:10.1002/cpa.3160481201.
URL <http://doi.wiley.com/10.1002/cpa.3160481201><http://onlinelibrary.wiley.com/doi/10.1002/cpa.3160481201/abstract>
- [64] A. Harten, P. D. Lax, B. van Leer, On upstream differencing and godunov-type schemes for hyperbolic conservation laws, *SIAM Review* 25 (1983) 35–61. doi:10.1137/1025002.
URL <http://epubs.siam.org/doi/10.1137/1025002>
- [65] N. Fleischmann, S. Adami, N. A. Adams, A shock-stable modification of the hllc riemann solver with reduced numerical dissipation, *Journal of Computational Physics* 423 (2020) 109762. doi:10.1016/j.jcp.2020.109762.
URL <https://doi.org/10.1016/j.jcp.2020.109762>
- [66] M. S. Liou, A sequel to ausm: Ausm+, *Journal of Computational Physics* 129 (1996) 364–382. doi:10.1006/jcph.1996.0256.
- [67] P. L. Roe, Approximate riemann solvers, parameter vectors, and difference schemes, *Journal of Computational Physics* 43 (1981) 357–372. doi:10.1016/0021-9991(81)90128-5.
- [68] S. F. Davis, Simplified second-order godunov-type methods, *SIAM Journal on Scientific and Statistical Computing* 9 (1988) 445–473. doi:10.1137/0909030.
URL <http://epubs.siam.org/doi/10.1137/0909030>
- [69] B. Einfeldt, On godunov-type methods for gas dynamics, *SIAM Journal on Numerical Analysis* 25 (1988) 294–318. doi:10.1137/0725021.
- [70] F. Acker, R. B. Borges, B. Costa, An improved weno-z scheme, *Journal of Computational Physics* 313 (2016) 726–753. doi:10.1016/j.jcp.2016.01.038.
URL <http://dx.doi.org/10.1016/j.jcp.2016.01.038>

- [71] N. R. Gande, A. A. Bhise, Modified third and fifth order weno schemes for inviscid compressible flows, *Numerical Algorithms* (2020). doi:10.1007/s11075-020-01039-9.
- [72] D. A. Bezgin, S. J. Schmidt, N. A. Adams, WENO3-NN: A maximum-order three-point data-driven weighted essentially non-oscillatory scheme, *Journal of Computational Physics* 452 (2022) 110920. doi:10.1016/j.jcp.2021.110920.
- [73] X. Y. Hu, Q. Wang, N. A. Adams, An adaptive central-upwind weighted essentially non-oscillatory scheme, *Journal of Computational Physics* 229 (2010) 8952–8965. doi:10.1016/j.jcp.2010.08.019.
URL <http://linkinghub.elsevier.com/retrieve/pii/S0021999110004560>
- [74] X. Hu, N. Adams, Scale separation for implicit large eddy simulation, *Journal of Computational Physics* 230 (2011) 7240–7249. doi:10.1016/j.jcp.2011.05.023.
URL <http://linkinghub.elsevier.com/retrieve/pii/S0021999111003342>
- [75] D. S. Balsara, C. W. Shu, Monotonicity preserving weighted essentially non-oscillatory schemes with increasingly high order of accuracy, *Journal of Computational Physics* 160 (2000) 405–452. doi:10.1006/jcph.2000.6443.
- [76] L. Fu, X. Y. Hu, N. A. Adams, A family of high-order targeted eno schemes for compressible-fluid simulations, *Journal of Computational Physics* 305 (2016) 333–359. doi:10.1016/j.jcp.2015.10.037.
- [77] B. van Leer, Towards the ultimate conservative difference scheme. v. a second-order sequel to godunov’s method, *Journal of Computational Physics* 32 (1979) 101–136. doi:10.1016/0021-9991(79)90145-1.
URL <https://linkinghub.elsevier.com/retrieve/pii/0021999179901451>
- [78] G. Russo, P. Smereka, A remark on computing distance functions, *Journal of Computational Physics* 163 (2000) 51–67. doi:10.1006/jcph.2000.6553.
URL <http://www.idealibrary.com>
- [79] S. Hickel, C. P. Egerer, J. Larsson, Subgrid-scale modeling for implicit large eddy simulation of compressible flows and shock-turbulence interaction, *Physics of Fluids* 26 (10) (2014). doi:10.1063/1.4898641.
- [80] P. Batten, N. Clarke, C. Lambert, D. M. Causon, On the choice of wavespeeds for the hllc riemann solver, *SIAM Journal on Scientific Computing* 18 (1997) 1553–1570. doi:10.1137/S1064827593260140.
URL <http://epubs.siam.org/doi/10.1137/S1064827593260140>

- [81] X. Y. Hu, B. C. Khoo, An interface interaction method for compressible multifluids, *Journal of Computational Physics* 198 (2004) 35–64. doi:10.1016/j.jcp.2003.12.018.
URL <http://linkinghub.elsevier.com/retrieve/pii/S0021999104000178>